

Bifurcation of planetary building blocks during Solar System formation

TIM LICHTENBERG,¹ JOANNA DRAŹKOWSKA,² MARIA SCHÖNBÄCHLER,³ GREGOR J. GOLABEK,⁴ AND THOMAS O. HANDS⁵

¹*Atmospheric, Oceanic and Planetary Physics, Department of Physics, University of Oxford, United Kingdom*

²*University Observatory, Faculty of Physics, Ludwig-Maximilians-Universität München, Germany*

³*Institute for Geochemistry and Petrology, Department of Earth Sciences, ETH Zurich, Switzerland*

⁴*Bayerisches Geoinstitut, University of Bayreuth, Germany*

⁵*Institute for Computational Science, University of Zurich, Switzerland*

Submitted 2 March 2020; Accepted 10 December 2020; Published 21 January 2021 ([Science 371, 6527](#))

ABSTRACT

Geochemical and astronomical evidence demonstrate that planet formation occurred in two spatially and temporally separated reservoirs. The origin of this dichotomy is unknown. We use numerical models to investigate how the evolution of the solar protoplanetary disk influenced the timing of protoplanet formation and their internal evolution. Migration of the water snow line can generate two distinct bursts of planetesimal formation that sample different source regions. These reservoirs evolve in divergent geophysical modes and develop distinct volatile contents, consistent with constraints from accretion chronology, thermo-chemistry, and the mass divergence of inner and outer Solar System. Our simulations suggest that the compositional fractionation and isotopic dichotomy of the Solar System was initiated by the interplay between disk dynamics, heterogeneous accretion, and internal evolution of forming protoplanets.

Planetary systems, including the Solar System, form by accretion from a protoplanetary disk of gas and dust. Astronomical observations of these disks provide evidence for rapid dust coagulation ([Segura-Cox et al. 2020](#)), show ringed substructure ([Andrews et al. 2018](#)), and indicate a decrease in total dust mass with disk age ([Ansdell et al. 2016](#)), to below the total masses in fully-assembled exoplanetary systems ([Najita & Kenyon 2014](#)). This suggests that planet formation starts early. At the onset of planetary accretion, small dust grains coagulate to form larger aggregates (pebbles). These pebbles drift inward under aerodynamic drag and gravitationally collapse when they reach sufficient local over-density ([Johansen et al. 2015](#)), which preferentially produces birth planetesimals of ≈ 100 km ([Delbo et al. 2017](#)). These bodies provide the seeds for the accretion process, but their direct growth by pebble accretion only becomes efficient after $\gtrsim 10^5$ – 10^6 yr, once they have grown to larger embryos through mutual collisions ([Liu et al. 2019](#)).

Meteorites record planet formation in our own Solar System and constrain the astronomical timescales: radiometric dating of meteorites suggests iron core formation (differentiation) in planetesimals by ≈ 1 Myr after the formation

of Ca,Al-rich inclusions (CAIs) ([Kruijjer et al. 2014](#)), the oldest known solids that formed together with the proto-Sun ([Connelly et al. 2012](#)). Core formation in first-generation, birth planetesimals is driven by internal radiogenic heating from ^{26}Al (half-life of $\sim 7 \times 10^5$ yr). Therefore, the time interval between planetesimal formation and differentiation ($\gtrsim 10^5$ – 10^6 yr) increases with later formation time, pointing to the formation of the earliest planetesimals in the inner Solar System $\lesssim 0.3$ Myr after CAI formation ([Kruijjer et al. 2014](#)). Combined, evidence from both astronomy and geochemistry suggests the onset of planet formation during the earliest phases of the solar protoplanetary disk.

Complementing astronomical evidence for disk substructure, meteorite data indicate spatial heterogeneity in the isotopic composition of planetary materials (*Supplementary Materials*): studies on Ti, Cr, Mo, and other isotope systems show variabilities across individual planetary bodies from different orbits ([Leya et al. 2008](#); [Trinquier et al. 2009](#); [Warren 2011](#)). Combined with temporal constraints on the accretion process, these divide the outer and inner Solar System reservoirs into chronologically and spatially distinct populations, also known as the carbonaceous chondrite (CC) and non-carbonaceous (NC) reservoirs, after their representative meteorite classes. The isotopic signatures record the heterogeneous distribution of presolar dust from multiple sites of stellar nucleosynthesis, and trace transport and mixing processes during

planet formation. In contrast, the elemental abundances and internal structure of planetary bodies were modified through geophysical evolution during planetary formation (Lichtenberg et al. 2019a). Earth’s nucleosynthetic isotope composition is NC-like and disparate from outer Solar System materials (*Supplementary Materials*), but its depletion pattern of moderately volatile elements is close to CCs (Braukmüller et al. 2019). This has been attributed to impact delivery (Schönbächler et al. 2010) or addition of pebbles (Schiller et al. 2018). The inner Solar System planets are depleted in highly volatile elements, such as hydrogen, carbon, and nitrogen, which influenced the availability of surface water and the composition of their atmospheres. This has been linked with the accretion of the terrestrial planets inside the snow line, where water ice is not stable during the disk phase, and later delivery of volatile-rich, outer Solar System materials (Peslier et al. 2018; Raymond et al. 2020).

The observed CC/NC dichotomy has been suggested to result from an early formation of proto-Jupiter $\lesssim 1$ Myr after CAI formation, which would inhibit the aerodynamic drift of dust grains and prevent initially heterogeneous disk materials from mixing (Kruijer et al. 2017; Desch et al. 2018). This scenario constrains the chronology and physical mechanism of Jupiter’s growth (Alibert et al. 2018), but potentially contradicts astronomical and geochemical evidence on the accretion process (*Supplementary Materials*).

FORMATION OF TWO DISTINCT PLANETESIMAL POPULATIONS

Multiple planetesimal populations can be formed during the build-up and evolution of the solar protoplanetary disk (Drażkowska & Dullemond 2018). We test whether such multi-stage planetesimal formation is consistent with the accretion chronology as inferred from meteorites. We use the output of previous simulations (Drażkowska & Dullemond 2018, see *Supplementary Materials*) to explore the CC/NC dichotomy. The simulations cover the initial infall and build-up of gas and dust, during which the disk itself accretes from the surrounding molecular cloud (Class I), and include the drift, coagulation and compositional evolution of the dust, and viscous evolution of the gas during the later evolutionary stage of the disk (Class II). In these simulations, the initial material accretes onto the innermost regions and continuously feeds more distant orbits through viscous expansion of the disk. The snow line moves outward during the Class I stage because a dense, compact disk forms, which heats up viscously. With the onset of the Class II stage, the gas density decreases, the temperature structure becomes dominated by stellar irradiation, and the snow line moves inward again.

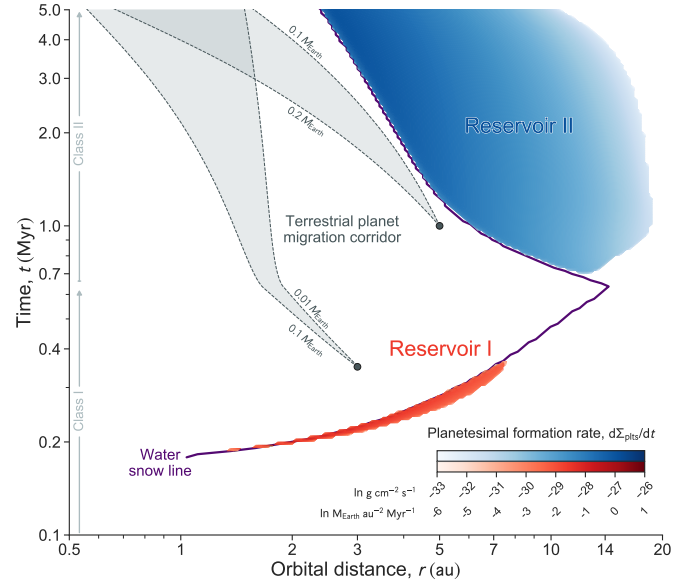


Figure 1. Formation of two distinct planetesimal populations in the disk simulation. The rate of planetesimal formation (change in surface density per timestep) is shown on logarithmic scale in cgs and natural units. The solid purple line indicates the orbital migration of the snow line, red and blue areas highlight the formation regions of the two planetesimal populations (Reservoir I and Reservoir II). The dashed gray lines (labeled ‘Terrestrial planet migration corridor’, cf. Fig. S10) bound the range of possible planet migration scenarios consistent with the present-day orbits of the terrestrial planets. While smaller embryos move slowly inward, more rapidly accreting (and thus more massive) embryos would migrate faster toward the proto-Sun. The light gray arrows on the left side indicate the transition from the Class I to Class II disk stage.

The snow line location affects the redistribution of dust grains. These are initially well-mixed with the disk gas, but radially drift due to coagulation and aerodynamic drag from the ambient gas. Inward-drifting, icy pebbles undergo rapid dehydration and size reduction at the snow line, which reduces their drift velocity and causes a pile-up of solid material. Outward diffusion of water vapor additionally leads to its recondensation onto icy grains beyond the snow line (the cold-finger effect), locally increasing the density of solids. When the conditions for the formation of dense, gravitationally unstable dust filaments (the streaming instability) are met in the simulation, planetesimals are formed. Planetesimal formation in the simulation preferentially occurs around the snow line. At 5 Myr into the simulation, which is the approximate upper lifetime of the solar nebula (*Supplementary Materials*), we assume that the gas disk dissipates and planetesimal formation halts.

In wind-driven disks with low levels of midplane turbulence the global angular momentum transport is dominated by near-surface layers (*Supplementary Materials*).

In this scenario, the outward-inward tacking snow line generates two distinct episodes of planetesimal formation in different orbital regions and time intervals (Fig. 1). The first, early-formed planetesimal population (hereafter Reservoir I) is triggered by the cold-finger effect between ≈ 0.2 – 0.35 Myr at orbital locations between ≈ 1.3 – 7.5 astronomical units (au) from the inside-out. The second planetesimal population (Reservoir II) mainly arises from large-scale inward-drift and pebble pile-up at the snow line in the Class II stage. This second population starts forming from ≈ 0.7 Myr between ≈ 17 – 3 au and proceeds from the outside-in. Due to differences in mechanism efficiency and local dust available, the two reservoirs differ substantially in their total formed mass: Reservoir I forms on the order of an Earth mass, Reservoir II forms on the order of a Jupiter mass in planetesimals (Drażkowska & Dullemond 2018, see *Supplementary Materials*). The build-up of both reservoirs depends on the local evolution of the pebble flux, but in turn influences the coagulation and drift of pebbles toward the inner disk (Figs. S1–S3). We therefore assess the feedback between reservoir formation and continuing planetary accretion.

HETEROGENEOUS ACCRETION AND RESERVOIR SEPARATION

We aim to determine the dominant mode of solid mass transfer in this disk build-up scenario, and to evaluate its consistency with the timescales of planetary accretion derived from radiometric ages (Rudge et al. 2010; Dauphas & Pourmand 2011; Kruijer et al. 2014). To relate the numerical simulation to geochemical chronology, we equate time zero in the disk model with the time of CAI formation (Connelly et al. 2012, *Supplementary Materials*). For fixed orbits at 2 and 15 au, approximately representative of Reservoir I and II in the inner and outer disk, we evaluate the anticipated growth timescales for two scenarios of protoplanet accretion (*Supplementary Materials*). We first consider collisional growth due to planetesimal-planetesimal interactions, during which the largest planetesimals grow by accreting smaller bodies. Second, we investigate the efficacy of pebble accretion, which is driven by the abundance of dust grains that cross the protoplanet orbit. Consistent with dynamical evidence from the asteroid-belt (Delbo et al. 2017) and numerical simulations of the streaming instability (Johansen et al. 2015), we assume a maximum planetesimal radius of 300 km, and that collisional growth is dominated by planetesimals of 50 km in radius. The orbit- and time-dependent evolution of the pebble flux (i.e., the transfer of solid mass in the disk), pebble size, and the gas disk characteristics are self-consistently derived from the disk and coagulation simu-

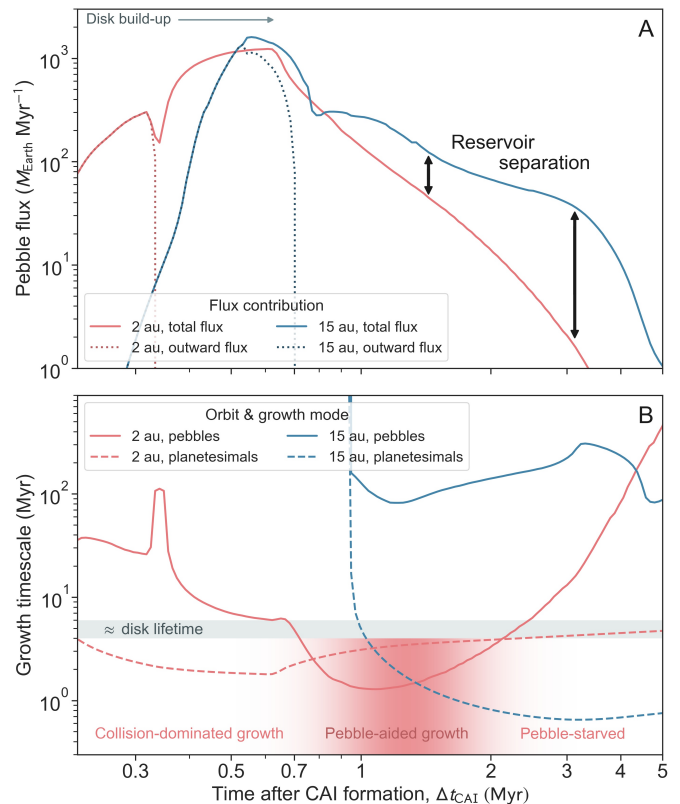


Figure 2. Pebble flux and planetesimal growth timescales in the disk simulation. (A) Pebble flux at 2 (red) and 15 (blue) au over time. During the disk build-up stage, the pebble flux is dominated by outward-moving dust (dotted lines), after which the pebbles start drifting inward. Reservoir I and II in the simulation progressively diverge in pebble flux by more than one order of magnitude due to accretion of Reservoir II (black arrows, labeled ‘Reservoir separation’). (B) Comparison of growth timescales for birth-sized planetesimals of 300 km radius by either pebble or planetesimal (collisional) accretion (*Supplementary Materials*) within the approximate lifetime of the solar protoplanetary disk (gray horizontal band, labeled ‘ \approx disk lifetime’). The red shaded area in the bottom indicates the time interval during which pebble accretion is more effective than collisional growth (labeled ‘Pebble-aided growth’, cf. Fig. S11).

lation described above (Drażkowska & Dullemond 2018, *Supplementary Materials*).

Under these conditions, the pebble flux is dominated by outward-moving dust grains (Fig. 2A) between ≈ 0.2 – 0.35 Myr after CAI formation because the disk accretes and viscously expands during the infall stage. The associated outward-directed pebble flux that passes Reservoir I is not efficient enough to drive substantial growth via pebble accretion, but planetesimal-planetesimal interactions lead to substantial growth within the timescale of disk evolution (Fig. 2B). Between ≈ 0.35 – 1 Myr, inward-drifting pebbles reach the inner disk, producing approximately equal contributions to accretion from both pebbles and collisions once

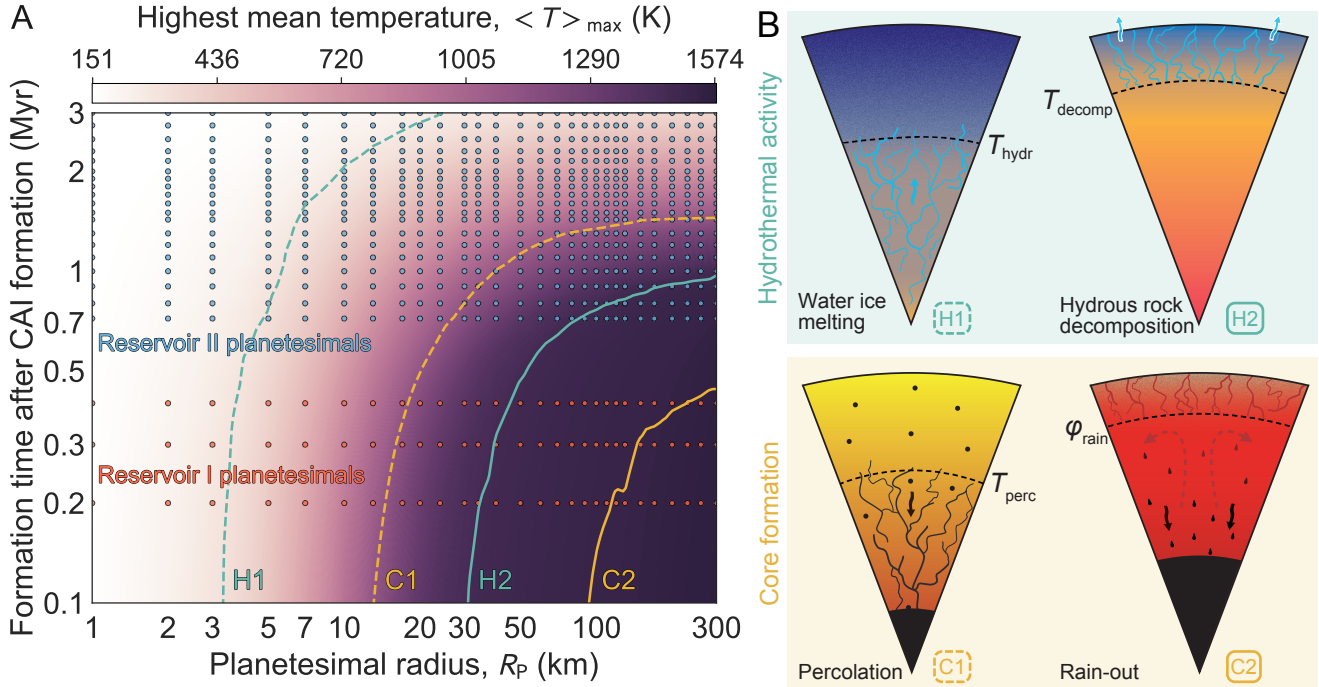


Figure 3. Simulated thermochemical evolution of planetesimals. (A) Highest mean internal temperature (color bar), interpolated from simulated planetesimal radii and formation times (dots). Reservoir I and II in the disk model are indicated by red and blue dots, respectively (cf. Fig. 1). Green and yellow lines (labeled H1–C2) indicate bodies for which 50 vol% (dashed lines) or 90 vol% (solid lines) of their interiors undergo hydrothermal activity (H1, H2) and iron core formation (C1, C2). (B) Schematic illustration of the scenarios indicated by the lines in panel A at peak heating and the threshold parameters (see main text and *Supplementary Materials*) to distinguish between regimes. H1, H2: Dark and light blue represent water ice and liquid water, respectively. Silicates are colored yellow to orange, indicating increasing temperature. Dashed black lines indicate the thresholds for water ice melting (T_{hydr}) and hydrous rock decomposition (T_{decomp}). The light blue arrows indicate hydrothermal circulation (H1) or degassing of volatiles (H2). C1, C2: Dark gray represents Fe,Ni–S metals. Silicates are colored yellow to red, indicating increasing temperature (yellow to orange) and progressive melting (red). Dashed black lines indicate the thresholds for metal percolation (T_{perc}) and rain-out (φ_{rain}). Dark gray arrows indicate core formation by percolation (C1) or rain-out (C2). Dark red dashed arrows (C2) indicate convection in the internal magma ocean.

the disk transitions into the Class II stage (Fig. 1). Subsequently, pebbles substantially contribute to planetesimal growth for a time interval of ≈ 1 Myr.

A final disk phase occurs from ≈ 2 Myr after CAI formation until gas disk dispersal, during which planetesimal growth by pebbles in Reservoir I stalls (*Supplementary Materials*). This is because a substantial fraction of solids, which drift from the outer toward the inner disk, are trapped in Reservoir II, where the pebbles gravitationally collapse to form planetesimals starting from ≈ 1 Myr after CAI formation onward (Fig. 2A). The build-up and onset of planetary accretion in Reservoir II shields Reservoir I from drifting grains that originate at larger orbital distances. The difference in pebble flux between the inner and outer Solar System reaches more than an order of magnitude. The pebble flux in the inner Solar System decreases to less than one Earth mass per million years after 3 Myr after CAI formation (Fig. 2A).

DIVERGENT GEOPHYSICAL EVOLUTION OF PLANETESIMAL POPULATIONS

These simulation results suggest that both planetesimals and pebbles contribute to planetary accretion. Rocky protoplanets that form from the planetesimal populations in both reservoirs inherit geochemical and geophysical properties from their precursor bodies (Lichtenberg et al. 2019a). The two planetesimal reservoirs differ substantially in accretion time and thus in radiogenic, internal heating from the decay of short-lived ^{26}Al . Meteorite data have shown that ^{26}Al heating in early-formed Solar System planetesimals drove their internal evolution, and thus altered their structure and bulk composition (Sutton et al. 2017; Alexander et al. 2018, *Supplementary Materials*). Therefore, we determine the internal and compositional evolution of the Reservoir I and II planetesimal populations formed in the disk simulation. We constrain the timing of iron core formation and hydrothermal activity (aqueous alteration and degassing) using geodynamic simulations of the thermochemical evolution of planetesimals. Our nu-

merical setup assumes isolated planetesimals that form instantaneously and evolve according to a fluid mechanical model (Lichtenberg et al. 2019a, 2018, *Supplementary Materials*).

We perform 700 single-planetesimal simulations, spanning the parameter range of planetesimal formation time, $t_{\text{form}} \in [0.1, 3.0]$ Myr, and planetesimal radius, $R_{\text{P}} \in [1, 300]$ km (Fig. 3A). To quantify their compositional evolution, we employ four thermochemical criteria (Fig. 3B) to determine the onset and cessation of core formation and hydrothermal activity (*Supplementary Materials*). Core formation in planetesimals initiates with the percolation of Fe,Ni-S liquids before silicate melting occurs, and terminates once the interior is sufficiently melted to form an internal magma ocean. At this stage metal droplets rain out from the convecting magma flow, producing complete differentiation between the metal core and liquid silicate mantle (Lichtenberg et al. 2018). Quantitatively, we assume that core formation occurs in regions with temperatures T higher than the threshold for metal-sulfide percolation, $T_{\text{perc}} \equiv 1273$ K, and completes for silicate melt fractions φ above the rheological transition, $\varphi_{\text{rain}} \equiv 0.4$, where rocks start to behave like a liquid rather than a solid. As temperature limits on hydrothermal (water-rock) activity, we assume water ice melts above $T_{\text{hydr}} \equiv 273$ K, and hydrous rock phases fully decompose above $T_{\text{decomp}} \equiv 1223$ K.

Averaged over the planetesimal volume, Fig. 3A indicates that larger and earlier-formed planetesimals experience higher temperatures during their evolution, leading to a greater degree of internal processing. Compared to Reservoir II, Reservoir I planetesimals reach systematically higher temperatures and undergo body-wide metal-silicate segregation. Reservoir I bodies larger than about 30 km in radius also reach near-complete dehydration. Reservoir II planetesimals only experience limited degrees of heating and therefore less core formation and dehydration. The peak temperatures (Fig. 3) only reveal approximate trends in the simulations, as heating and compositional evolution are highly variable on timescales of 10^5 – 10^6 yr (Figs. S4–S7).

To compare the simulations with the meteorite record, we explore the time-dependent evolution of the planetesimal populations in both reservoirs. We assume the planetesimal number distributions follow that of the streaming instability (*Supplementary Materials*) in the interval $R_{\text{P}} \in [1, 300]$ km, and take into account the generation of new planetesimals in the simulation. We then evolve the birth planetesimal populations in Reservoir I and II and derive the fraction of each reservoir that falls within the threshold criteria, normalized to the final reservoir population after 5 Myr in the disk simulation.

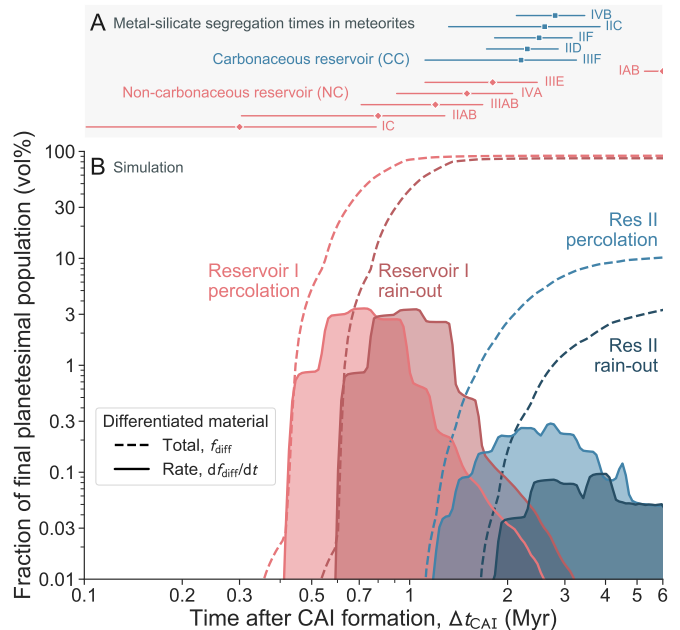


Figure 4. Comparison of metal-silicate separation times in simulated planetesimal populations with the meteorite record. (A) Metal-silicate separation times in NC and CC meteorite classes (Tab. S1). (B) Timing of core formation in Reservoir I (red) or Reservoir II (blue). Solid lines with colored shading represent the fraction of material undergoing metal-silicate separation (cf. Fig. 3 and *Supplementary Materials*). Dashed lines show the total volumetric fraction for each scenario over time. Light and dark red/blue indicate percolation or rain-out, respectively.

Fig. 4 compares the radiometric ages of metal-silicate separation in meteoritic measurements with the thermochemical evolution in our simulations. Reservoir I planetesimals undergo core formation between ≈ 0.4 – 3.0 Myr after CAI formation, with a peak between ≈ 0.6 – 1.3 Myr. On average, core formation via percolation occurs ≈ 0.4 Myr earlier than via rain-out in internal magma oceans. Multi-stage core formation scenarios, in which cores form by multiple stages of percolation and rain-out, are bracketed by these time intervals. Reservoir II planetesimals undergo core formation at later stages, starting at ≈ 1.1 Myr after CAI formation for percolation, and at ≈ 1.8 Myr after CAI formation for rain-out, and peaking between ≈ 1.8 – 3.1 and ≈ 2.3 – 4.0 Myr, respectively. The peak interval and the fraction of material experiencing differentiation in Reservoir I is earlier and higher than in Reservoir II due to the differing formation times and thus varying initial abundance of ^{26}Al . The timing of core formation in both simulated populations agree with the meteorite data within the uncertainties of the individual ages (Kruijer et al. 2014, 2017; Hunt et al. 2018). The spread in early-formed NCs is reproduced within the uncertainties, with the exception of

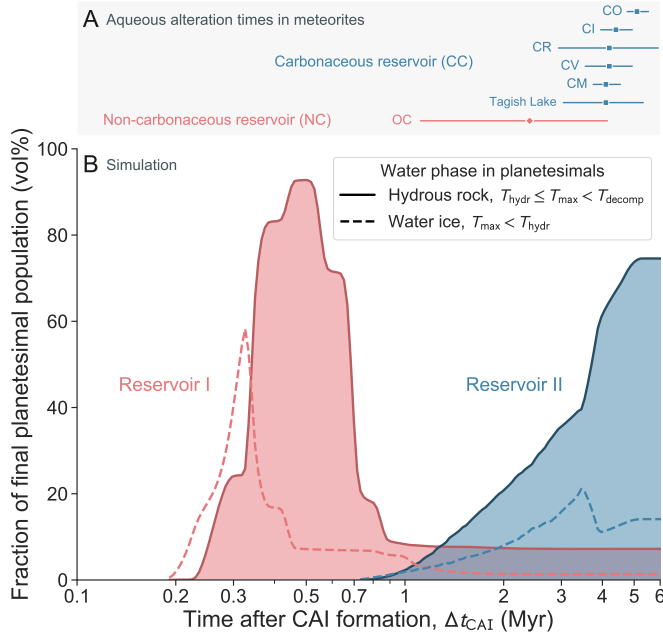


Figure 5. Comparison of hydrothermal activity in simulated planetesimal populations with aqueous alteration times in the meteorite record. (A) Aqueous alteration times in NC and CC meteorite classes (Tab. S1). **(B)** Fraction of planetary materials that retain primordial water ice (dashed lines) or undergo hydrothermal activity and retain water in hydrous silicate phases (solid lines with colored shading) in the simulations.

the IAB meteorite group (Hunt et al. 2018). The fractional volumes in both simulated reservoirs differ, with ≈ 2 –10 vol% of Reservoir II undergoing core formation, whereas Reservoir I planetesimals differentiate to $\gtrsim 90$ vol%.

Fig. 5 compares aqueous alteration ages from meteorites with our simulations. Simulated planetesimals in Reservoir I experience a brief phase of hydrothermal activity between ≈ 0.25 –0.7 Myr after CAI formation and then dehydrate rapidly at ≈ 0.7 Myr. After that initial peak of water ice melting and hydrothermal activity, ≈ 10 vol% of rock contains hydrous silicate phases, and $\lesssim 1$ vol% of water ice is retained. Reservoir II planetesimals, which form later with less ^{26}Al , experience protracted hydrothermal activity lasting for several Myr with a peak at ≈ 5 Myr after CAI formation. At ≈ 3.5 Myr after CAI formation, more than 50 vol% of the Reservoir II planetesimals have undergone hydrothermal activity. At ≈ 5 Myr after CAI formation, the simulation reaches a steady-state with ≈ 15 vol% water ice and ≈ 75 vol% hydrous rock. The peak for hydrothermal activity in Reservoir II reproduces the clustering of aqueous alteration in the CC meteorite record. The single available age for the NC population (an ordinary chondrite, OC) does not coincide with the peak in the Reservoir I population, which we discuss below.

COMPOSITIONAL DICHOTOMY BETWEEN INNER AND OUTER SOLAR SYSTEM

Our simulations indicate that the formation of spatially and temporally distinct planetesimal populations resulted in differing evolutionary pathways for planet formation in the inner and outer Solar System. The initial seed population of the inner Solar System planets formed during the infall stage, while the outer Solar System planetesimal population started to form later, at the beginning of the Class II disk stage. Fig. 6 shows our interpretation of the isotopic evolution during early Solar System formation. Measurements of CAIs indicate that the earliest Solar System infall material was initially dominated by dust enriched in supernovae-derived isotopes, then transitioned to a more depleted isotopic composition (Desch et al. 2018; Nanne et al. 2019; Jacquet et al. 2019). The distribution of isotopes evolved with time because of viscous disk spreading and increasing specific angular momentum of infalling matter. As a result, the outer disk became progressively dominated by early-infalling, enriched material, whereas the inner disk became dominated by late-infalling, depleted material (Desch et al. 2018; Nanne et al. 2019; Jacquet et al. 2019). We suggest that the distinct NC and CC reservoirs measured in the meteorite record result from the combined influence of early planetesimal formation in the inner Solar System and the subsequent dust pile-up at the snow line. The latter effect suppressed the rapid inward drift of enriched material and prevented isotopic homogenization of the disk. It also led to the onset of planetesimal formation and planetary accretion in the outer Solar System, which further limited mixing by dust drift from the outer to the inner reservoir.

Fig. 6 also illustrates our proposed timeline of compositional evolution and accretion, based on our simulations. The first planetesimal population formed due to the cold-finger effect. These bodies incorporated a substantial amount of ^{26}Al and thus dehydrated and differentiated rapidly. Initial growth in the inner Solar System proceeded from mutual collisions among planetesimals to an intermediate phase of pebble accretion. During the final phase before disk dissipation, the pebble flux in the inner Solar System diminished and pebble growth may have stalled (see below). The outer Solar System population began to form later, during the Class II disk stage, and incorporated more total dust mass into its planetesimals. The initial phase of collisional growth was then succeeded by pebble accretion. This series of growth stages proceeded faster than in the inner Solar System due to the higher local pebble flux.

This chronology is consistent with meteoritic and astronomical evidence and makes several potentially testable predictions. The rapid decrease in the pebble flux in the inner Solar System (Reservoir I), to less than one Earth

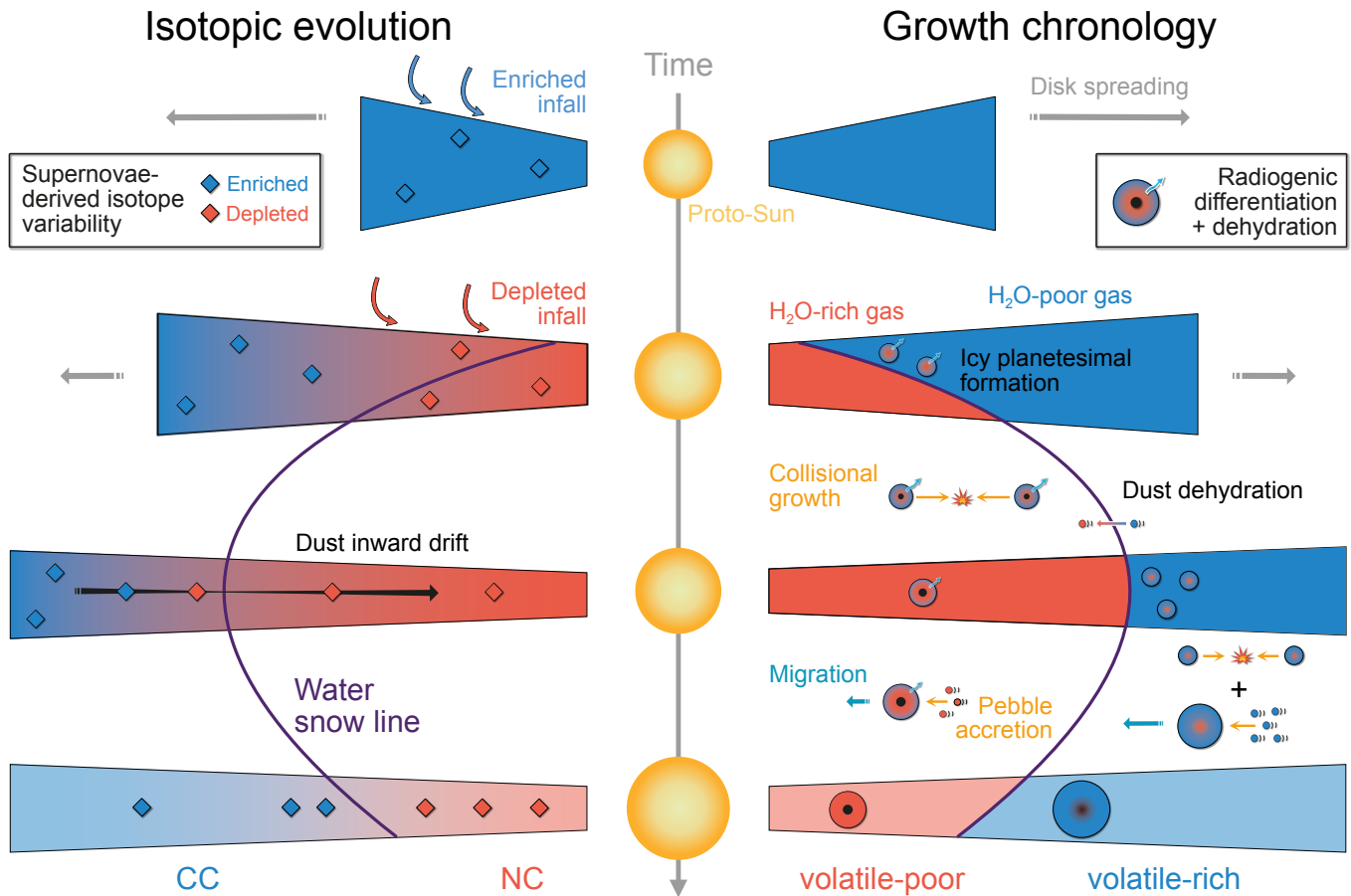


Figure 6. Schematic illustration of our proposed chronology of early Solar System accretion. Nucleosynthetic isotope variability (left) across the disk due to varying composition of infall material is retained by the pile-up of inward-drifting dust grains at the snow line. The formation of two distinct planetesimal populations initiates divergent evolutionary pathways of inner and outer Solar System (right) due to the secular variation of local material composition, internal radiogenic heating, and dominant mode of planetary growth.

mass per Myr, reduces the growth by pebble accretion during later disk stages. Parameter space exploration (*Supplementary Materials*) and previous work (Levison et al. 2015) indicate that under such conditions pebble accretion onto inner Solar System planetary embryos is inefficient. This implies that the intermediate, pebble-driven accretion phase stalled, and subsequent growth of the terrestrial protoplanets was driven by collisional interactions during the final disk stages and afterwards. Such protracted accretion timescales for the terrestrial planets are supported by radiometric evidence for both proto-Earth and proto-Mars (Dauphas & Pourmand 2011; Rudge et al. 2010), and the absence of rocky planets larger than Earth (super-Earths) in the inner Solar System. The formation of super-Earth exoplanets has been attributed to a high pebble flux and rapid inward migration with increasing planet mass (Raymond et al. 2020; Bitsch et al. 2019b; Liu et al. 2019, *Supplementary Materials*). The secular transition of an early, low pebble flux to a brief period of high pebble flux could amplify preceding mass differences between accreting protoplanets and thus explain why Earth is the

inner Solar System body with the closest composition to CI-chondrites (Trinquier et al. 2009; Schönbachler et al. 2010; Schiller et al. 2018; Braukmüller et al. 2019).

The secular transition between growth regimes, the internal evolution of planetesimals, and the temporal variation of the local pebble composition would lead to a heterogeneous delivery of water and other highly volatile compounds to the inner Solar System (*Supplementary Materials*): the birth planetesimals in Reservoir I form an initial seed-population of water-rich bodies that subsequently dehydrate from ^{26}Al heating and accrete via collisions. With progressing time and planetary growth, the protoplanets in the inner Solar System experience an influx of dry pebbles between $\approx 1\text{--}2$ Myr after CAI formation. Forming such initially icy and subsequently dehydrating planetesimals in the inner Solar System is consistent with measurements of hydrogen content in enstatite (Piani et al. 2020), carbonaceous chondrite (Piani et al. 2018), eucrite and angrite (Sarafian et al. 2017) meteorites, Earth's deep mantle, and bulk measurements of the terrestrial planets and asteroid families (Peslier et al.

2018; Alexander et al. 2018). The timing of hydrothermal activity in Reservoir I planetesimals in our simulations, at $\approx 0.3\text{--}0.7$ Myr after CAI formation, is offset from the Reservoir II peak at $\gtrsim 4$ Myr after CAI formation (Fig. 5). Most of the hydrous phases that are formed in the Reservoir I peak, however, are subsequently destroyed by high-temperature internal processing in our simulations, consistent with evidence from NC meteorites (Lewis & Jones 2016). Such intense (planetary) thermal processing in Reservoir I may thus lead to fractionation in mass-dependent isotopes (Benedikt et al. 2020), consistent with evidence from terrestrial planetary bodies (Hin et al. 2017; Norris & Wood 2017). The disk simulation does not produce direct analogues of ordinary or enstatite chondrites from gravitational collapse, but the predicted growth stages (Figs. 2 and 6) would lead to recycling of collisionally disrupted planetesimals (Lichtenberg et al. 2018) and secondary layers accreted onto growing bodies (Maurel et al. 2020), which could be potential origin locations. The formation of Reservoir II planetesimals with initially higher-than-today water abundances is consistent with evidence for extensive iron oxidation and deuterium enrichment during aqueous alteration of CC meteorites (Sutton et al. 2017). Simulated Reservoir II planetesimals undergo a prolonged Myr-long phase of hydrothermal activity with a peak at $\approx 4\text{--}5$ Myr after CAI formation, which reproduces the aqueous alteration ages of CC meteorites (Alexander et al. 2018). However, later-formed Reservoir II bodies remain almost unmodified by hydrothermal alteration (Fig. 3), so surviving bodies today should display varying internal processing, ranging from extensive aqueous alteration to fully pristine for small and late-formed bodies. Reservoir II planetesimals sample material originating from a wide range of orbital distances and form over an extended time interval. Therefore, compared to Reservoir I planetary materials, Reservoir II bodies may exhibit larger intra-reservoir isotope variability. This is consistent with the nucleosynthetic isotope variability (Leya et al. 2008) and abundance of presolar interstellar materials (Davidson et al. 2014) in carbonaceous chondrites, and the scatter in cometary D/H ratios (Alexander et al. 2018).

In summary, the chronology of Solar System formation (Fig. 6) we infer from our simulations links several characteristics found by geochemical laboratory analyses and astronomical observations. We interpret the chemical (volatile-poor versus volatile-rich) and isotopic (NC versus CC) dichotomy as causally linked by the build-up of distinct planetesimal populations in the inner and outer Solar System. Mixing by dust drift between them is limited to the earliest disk phases and declining with time due to the progressive accretion of the outer Solar System plan-

etary population. The temporal and spatial variation in the main volatile reservoirs and heterogeneous planet growth are intrinsically coupled to the disk structure, the redistribution and fractionation of volatile ices, the abundance of short-lived radionuclides, and the geophysical evolution of protoplanets during planetary formation.

Acknowledgements—We thank C. P. Dullemond, A. C. Hunt, I. Pascucci, S. Ida, J. Wade, S.-J. Paardekooper, T. Birnstiel, S. M. Stammer, J. J. Barnes, A. Morbidelli, W. Kley, and members of the ERC EXOCONDENSE project at Oxford for discussions; B. Liu (刘倍贝), J. F. J. Bryson, M. Ek, R. D. Alexander, and S. Charnoz for comments on earlier draft versions; T. V. Gerya for usage of the I2ELVIS code family; and C. P. Dullemond for usage of the disk evolution code. *FUNDING*: T.L. received funding from the Simons Foundation (SCOL award #611576) and the Swiss National Science Foundation (grant #P2EZP2-178621). J.D. received funding from the European Research Council under the European Union's Horizon 2020 research and innovation program (grant #714769). T.O.H. was supported by the University of Zurich Forschungskredit Postdoc. Parts of this work were carried out within the framework of the National Centre for Competence in Research PlanetS (grant #51NF40-141881) supported by the Swiss National Science Foundation. *AUTHOR CONTRIBUTIONS*: Conceptualization, T.L., J.D., M.S., G.J.G.; Methodology, T.L., J.D., T.O.H., G.J.G.; Software, T.L., J.D., T.O.H., G.J.G.; Validation, all authors; Formal Analysis, T.L., J.D., T.O.H.; Investigation, T.L., J.D., M.S.; Resources, T.L., J.D., M.S.; Writing, T.L., J.D., T.O.H., M.S.; Review & Editing, all authors; Visualization, T.L.; *COMPETING INTERESTS*: We declare no competing interests. *DATA AND MATERIALS AVAILABILITY*: Simulation codes and output data are available at osf.io/e2kfv.

SUPPLEMENTARY MATERIALS

MATERIALS & METHODS

DISK EVOLUTION & PLANETESIMAL FORMATION

Planetesimals, the gravitationally bound seeds of the accretion process and building blocks of planets, are thought to form in a multi-stage process with dust first growing to pebble sizes, which can then be concentrated by the streaming instability (Johansen et al. 2014). The streaming instability is a two-fluid mechanism driven by the relative flow of gas and dust which leads to the formation of dense dust filaments in circumstellar disks. Under certain conditions, those filaments may become massive enough to collapse under their own gravity, leading to rapid planetesimal formation (Youdin & Goodman 2005; Johansen et al. 2007). Planetesimals may be formed throughout the protoplanetary disk as long as both gas and pebbles are present to create localized overdensities that breach the physical conditions for gravitational collapse. To calculate the timing and integrated mass of planetesimals formed via the streaming instability, we consider a physical model of the nebular gas disk, dust evolution including growth and fragmentation (Birnstiel et al. 2016), and a prescription for turning pebbles into planetesimals that parameterizes the effects of gravitational collapse and planetesimal formation as obtained from fluid dynamical models.

We make use of previously-published simulations (Drażkowska & Dullemond 2018) that include a one dimensional model in which the protoplanetary disk is formed from the parent molecular cloud and undergoes viscous evolution. These simulations follow the rotating infalling cloud model (Hueso & Guillot 2005; Dullemond et al. 2006a,b). In this model there are essentially three components: the parent molecular cloud, which rotates as a solid body, the central star, and the disk, both of which are growing, fed by the infalling cloud. We use this simulation to follow the gas and dust evolution from the infall (Class I) to the Class II disk stage, for which there is observational evidence for declining dust mass with time (Ansdell et al. 2016; Pascucci et al. 2016; Andrews et al. 2018; Tychoniec et al. 2020). The disk simulation assumes an initial mass of 1 solar mass (M_{\odot}), an isotropic temperature of 10 K, and a rotation rate of $5 \times 10^{-15} \text{ s}^{-1}$ for the parent molecular cloud of the Solar System. After about $7 \times 10^5 \text{ yr}$ this cloud forms a single central star surrounded by a circumstellar disk with a peak total mass of $0.2 M_{\odot}$ (Fig. S1). The temperature of the disk is calculated taking into account heating due to viscosity and irradiation by the central star. The evolution of the gas surface density Σ_g (Fig. S2) is computed using

$$\frac{\partial \Sigma_g}{\partial t} + \frac{1}{r} \frac{\partial}{\partial r} (r \Sigma_g v_r) = S_g, \quad (\text{S1})$$

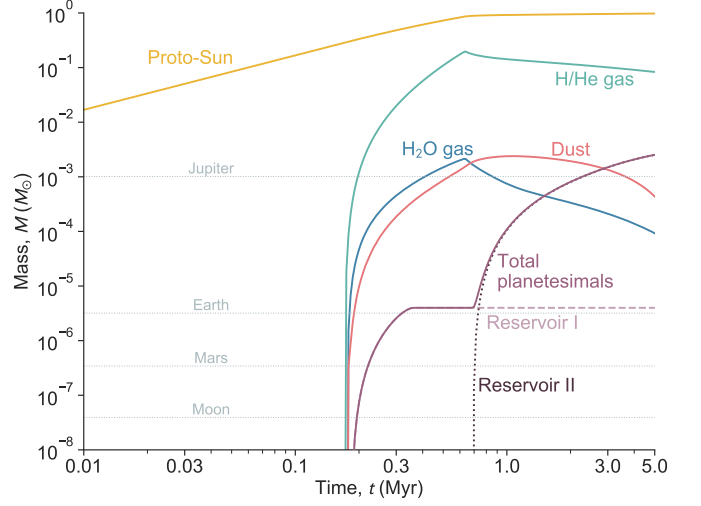


Figure S1. Mass evolution for different reservoirs in the disk simulation (Drażkowska & Dullemond 2018). The mass of the proto-Sun (yellow line), H/He gas (green), H_2O gas (blue), and dust (red) grow from the surrounding molecular cloud until the end of the Class I disk stage at $\approx 0.7 \text{ Myr}$. The mass in planetesimals (solid purple line) is divided into Reservoir I (dashed purple line) and Reservoir II (dotted purple line) as defined in Fig. 1. Overplotted are the present-day masses of several Solar System objects (horizontal lines).

where r denotes the radial distance to the central star, t the time, v_r is the radial velocity of the gas, and S_g represents a source term due to matter infalling onto the disk from the molecular cloud. The viscous evolution of gas follows the standard α -formalism (Shakura & Sunyaev 1973), where the gas viscosity is defined as

$$\nu = \alpha_v c_s H_g, \quad (\text{S2})$$

where c_s is the sound speed, H_g is the gas scale height, and α_v is the disk viscosity, parameterizing the physical mechanism of angular momentum transport of the disk. The viscosity is fixed to $\alpha_v = 10^{-3}$. We refer to (Drażkowska & Dullemond 2018) for the effects of a varying α_v on dust coagulation and planetesimal formation. The viscosity determines the radial gas velocity, which is calculated from

$$v_r = -\frac{3}{\Sigma_g \sqrt{r}} \frac{\partial}{\partial r} (\Sigma_g \nu \sqrt{r}). \quad (\text{S3})$$

The infall of gas is complemented by the delivery of dust (Fig. S3), with a dust-to-gas ratio of 1%, as found in the interstellar medium (Ferrière 2001). We follow the evolution of dust surface density Σ_d using the advection-diffusion equation,

$$\frac{\partial \Sigma_d}{\partial t} + \frac{1}{r} \frac{\partial}{\partial r} \left[r \left(\Sigma_d \bar{v} - \nu \Sigma_g \frac{\partial}{\partial r} \left[\frac{\Sigma_d}{\Sigma_g} \right] \right) \right] = S_d, \quad (\text{S4})$$

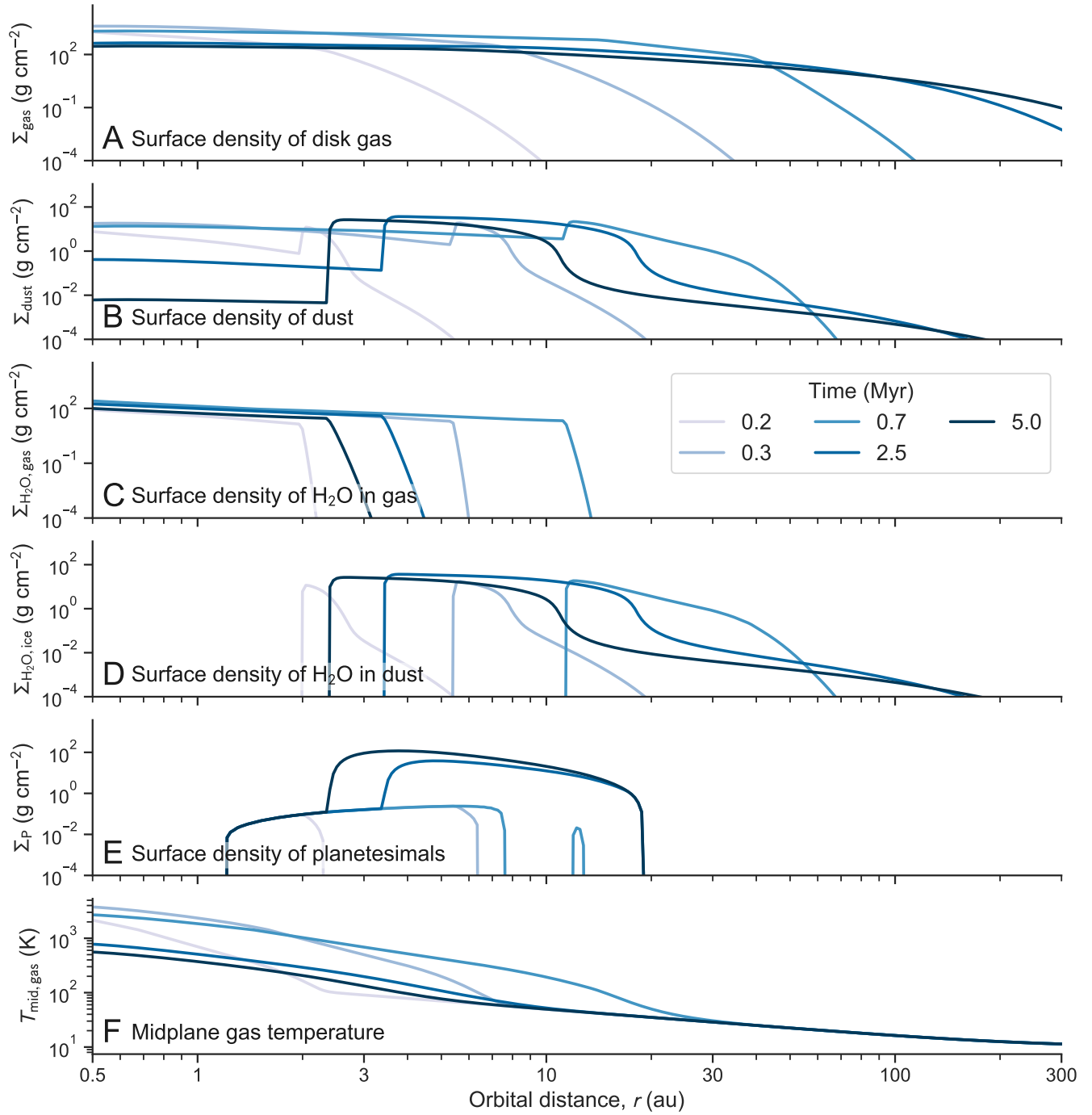


Figure S2. Radial distribution and time evolution of the composition in the disk simulation (Drażkowska & Dullemond 2018). Shown are the surface densities of H/He gas (A), dust (B), H_2O gas (C), H_2O ice (D), planetesimals (E), and midplane gas temperature at 0.2, 0.3, 0.7, 2.5, and 5.0 Myr (light to dark blue).

where S_d is the source term for the μm -sized dust infalling from the molecular cloud and \bar{v} is the mass-weighted averaged radial speed of dust grains, which depends on dust size. Dust and gas are assumed to be initially well-mixed. The dust grains start to decouple from the gas as they grow into larger (pebble) sizes. Dust grain growth is computed adopting an algorithm (Birnstiel et al. 2012) that relies on only tracking two populations of dust grains: the small and the large ones. Dust size is regulated by the initial growth phase and halted either by fragmentation or radial drift.

Alongside dust growth, ice sublimation and water vapor re-condensation are incorporated (Ciesla & Cuzzi 2006). The infalling dust is assumed to consist of 50% refractory material and 50% water ice. When the ice sublimates, its mass is added to the water vapor reservoir. For the gas disk content, the surface density of water vapour and hydrogen-helium is tracked separately. When the water vapor exceeds the equilibrium vapor pressure value, it condenses onto the existing grains, adding to their water ice content. In contrast, when the water vapor pressure is lower than the equilibrium pressure, sublimation takes place. This way, the position of the snow line can be measured as the location where the ice content of grains changes rapidly. The composition of grains alters their sticking properties such that ice-rich grains are more sticky compared to refractory, ice-free grains (Wada et al. 2009, 2011; Aumatell & Wurm 2014). Thus, the fragmentation threshold velocity for dry aggregates inside of the snow line is set to $v_{\text{frag, in}} = 1 \text{ m s}^{-1}$ and for icy aggregates outside of the snow line to $v_{\text{frag, out}} = 10 \text{ m s}^{-1}$.

Planetesimal formation is included by assuming that planetesimals form through the streaming instability when the midplane dust-to-gas ratio of pebbles, which are characterized by the Stokes number $\text{St} \geq 10^{-2}$, exceeds unity. Whenever this criterion is fulfilled, part of the surface density of pebbles is transferred into planetesimals. For this to take place, a dense midplane layer of sufficiently large pebbles is required. In the disk model, these large pebbles only grow outside of the water snow line, where the dust is more sticky. Enhancements of the vertically integrated dust-to-gas ratio to trigger planetesimal formation have been shown to build-up in the inner part of the protoplanetary disk during long-term dust evolution and mass influx from the outer parts of the disk (Drążkowska et al. 2016). The adopted disk model does not include a physical mechanism for gas disk dispersal, such as internal or external photoevaporation (Ercolano & Pascucci 2017), which can affect the total mass of planetesimals that are formed during the final stages of disk evolution. However, geochemical (Bollard et al. 2017) and paleomagnetic (Wang et al. 2017) proxies indicate a dispersal of the solar

nebula on the order of 4–5 Myr, which is when we assume the disk to disperse and planetesimal formation to cease.

We focus on the physical processes taking place around the snow line, which facilitates dust-to-gas overdensities as the dry dust inside of the snow line reaches smaller sizes and thus drifts more slowly than the icy dust outside, which leads to a pile-up effect (Ida & Guillot 2016; Drążkowska & Alibert 2017; Schoonenberg & Ormel 2017). However, the build-up of this enhancement similarly requires mass transfer from the outer to the inner disk on a timescale of $\gtrsim 10^5 \text{ yr}$, depending on the assumed disk parameters. Thus, planetesimal formation triggered by this mechanism typically takes place in the Class II disk stage (Drążkowska & Dullemond 2018). An additional mechanism that operates on shorter timescales, but also leads to less pronounced enhancement of dust density, is the cold-finger effect (Stevenson & Lunine 1988; Cuzzi & Zahnle 2004). This relies on the outward diffusion of water vapor from inside and its subsequent re-condensation onto the grains outside of the snow line. This mechanism produces a moderate enhancement of the vertically integrated dust-to-gas ratio during the protoplanetary disk build-up stage, and depends on the level of midplane gas turbulence.

In the adopted inside-out infall model, the snow line first moves outward during the infall phase, reaching its furthest location when the disk obtains its peak mass (at about 0.7 Myr) resulting from an increase in stellar luminosity and gas density during disk build-up (Fig. S2A). The temperature is calculated taking into account both the irradiation from the central star and dissipation of viscous energy by turbulence. Stellar irradiation sets a shallow temperature profile in the whole disk, while viscous heating increases the temperature dominantly in the inner parts, which leads to a steeper temperature profile close to the star compared to a profile with only irradiation (Fig. S2F). In the Class II phase, snow line movement is driven both by the evolution of the slowly cooling disk, and by dust evolution. The position of the snow line is self-consistently computed as the location at which the dust grains contain less than 1% ice component, thus the snow line evolution is an outcome rather than an assumption of the simulation. The pebble pile-up outside of the snow line (Figs. S2B and D) increases the time it takes the solid ice component of pebbles to evaporate while they drift inward. As a result, the snow line position moves inward faster than it would just from the temperature evolution.

The position of the snow line is related to the temperature structure, which in the inner disk is dominated by the dissipation of viscous energy by turbulence. From astronomical observations of other protoplanetary disks, the level of turbulence, and thus the major physical mecha-

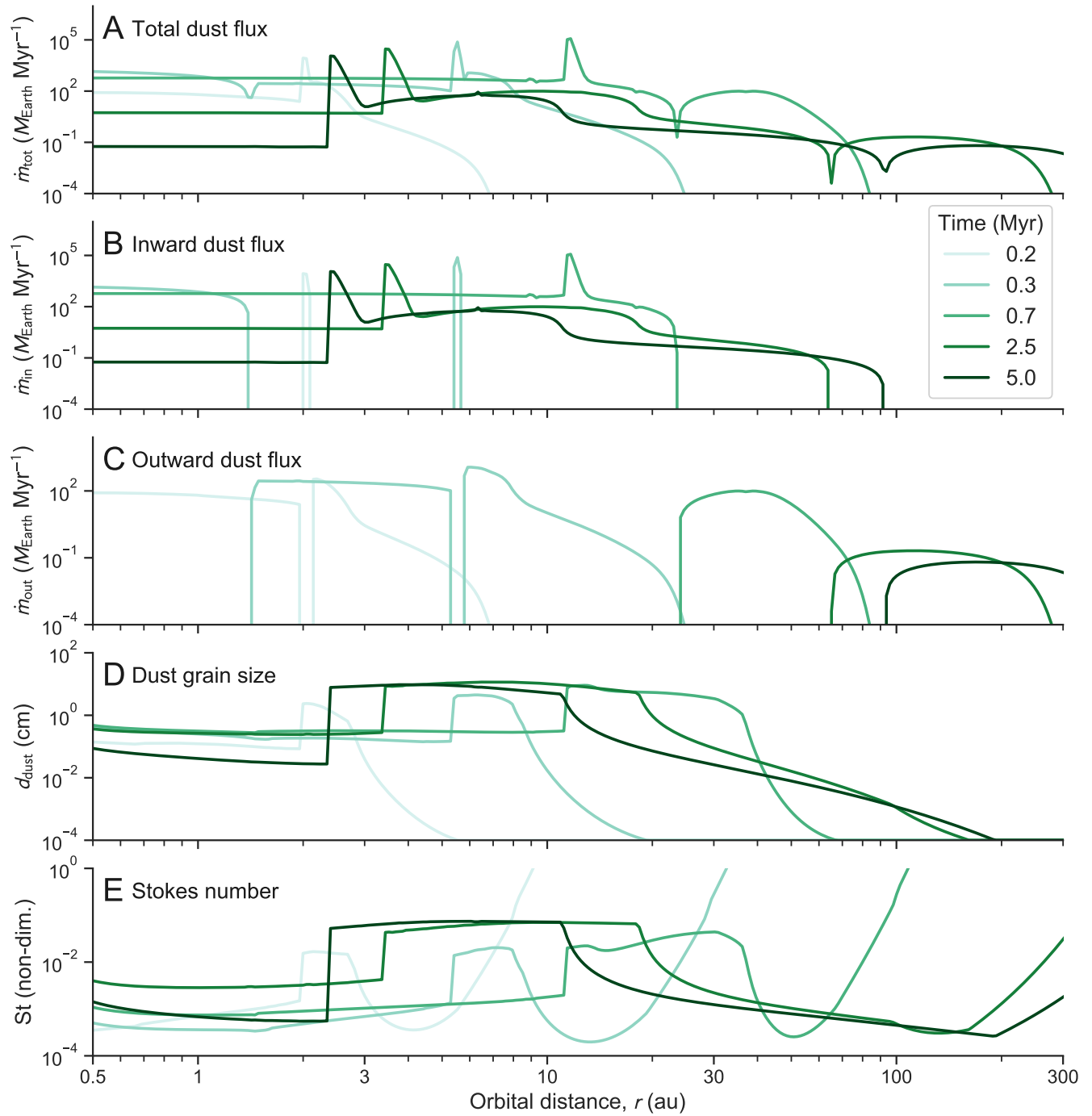


Figure S3. Radial distribution and time evolution of additional dust parameters in the disk simulation (Drażkowska & Dullemond 2018). Shown are total dust flux (A), inward dust flux (B), outward dust flux (C), dust grain size (D), and the Stokes number (E) at 0.2, 0.3, 0.7, 2.5, and 5.0 Myr (light to dark green).

nism of angular momentum transport, remains unclear. Some observational attempts to measure turbulence have been inconclusive (Flaherty et al. 2015; Teague et al. 2016). In a standard model of protoplanetary disk evolution (Balbus & Hawley 1991), the angular momentum transfer is driven by isotropic turbulence, such that the ratio of midplane turbulence (α_t) equals the disk viscosity, hence $\alpha_v = \alpha_t$. However, large regions of the protoplanetary disk, mostly surrounding its midplane, are expected to be free from turbulence (Gammie 1996). This is supported by observational evidence for turbulence levels that are lower than anticipated (Flaherty et al. 2017; Teague et al. 2019; Flaherty et al. 2020). The disk model we employ (Drążkowska & Dullemond 2018) mimics a disk structure in which the midplane turbulence is lower than that expected from the global angular momentum transport rate by decoupling the ratio of midplane turbulence, α_t , from the global viscous α -parameter, α_v . This is a simple mimicking of a potentially much more complex structure of a non-ideal magneto-hydrodynamic disk, in which large regions of the midplane are free from turbulence and the angular momentum can be removed vertically by magnetic winds or radially by laminar torques (Lesur et al. 2014; Bai et al. 2016; Bai 2017). Similar approaches were used in other recent models (Carrera et al. 2017; Ercolano et al. 2017). A parameter study of α_v and α_t space has been performed for this model (Drążkowska & Dullemond 2018), which concluded that early planetesimal formation in the infall stage is only possible if $\alpha_t \ll \alpha_v$ because planetesimal formation from the cold-finger effect is favoured by near-laminar midplane conditions. We focus on the scenario with $\alpha_t = 10^{-5}$ and $\alpha_v = 10^{-3}$ (Drążkowska & Dullemond 2018). However, our results would be qualitatively similar for any model forming planetesimals both during the infall and the disk stage.

Decoupling the α_v and α_t values aims to mimic the layered accretion scenario in which the gas flow takes place in active layers above a laminar midplane. However, the disk model is one dimensional and vertically integrated. Thus, α_v describes the density-averaged gas flow and is used to calculate the disk temperature in the viscous heating regime. This leads to intermittent high temperatures in the inner disk and pushes the water ice line to radii beyond 10 au for a short time interval. Calculating the midplane temperature is generally a complex radiative transfer problem (Turner et al. 2014) and numerical models vary in their conclusions on the midplane temperature in the inner parts of the disk (Flock et al. 2013; Schobert et al. 2019), associated dust redistribution and composition, and hence planetesimal formation rates (Sato et al. 2016; Charnoz et al. 2019; Ida et al. 2019).

THERMOCHEMICAL EVOLUTION OF PLANETESIMALS

Once planetesimals are formed in the disk model, we follow their internal evolution using published methodology (Lichtenberg et al. 2018, 2019a). We consider single planetesimals of radius R_P and instantaneous formation time t_{form} . The formation time defines the planetesimal internal heat budget assuming a disk-wide initial homogeneous ratio of $(^{26}\text{Al}/^{27}\text{Al})_{\text{CAI}} \equiv 5.25 \times 10^{-5}$ (Kita et al. 2013) at the time of CAI formation (Connelly et al. 2012), which defines our time zero.

Our numerical model of the thermochemical evolution of planetesimals builds on the fluid mechanical framework I2ELVIS (Gerya & Yuen 2003, 2007; Gerya 2019). We numerically solve the fluid dynamic conservation equations using the extended Boussinesq approximation (Gerya 2019) in a two-dimensional infinite cylinder geometry on a Cartesian grid, namely the continuity, Stokes, Poisson, and energy conservation equations,

$$\frac{\partial \rho}{\partial t} + \nabla \cdot \rho \mathbf{v} = 0, \quad (\text{S5})$$

$$\nabla \cdot \sigma' - \nabla P + \rho \mathbf{g} = 0, \quad (\text{S6})$$

$$\nabla^2 \Phi = 4\pi G \rho, \quad (\text{S7})$$

$$\rho c_P \left(\frac{\partial T}{\partial t} + v_i \cdot \nabla T \right) = - \frac{\partial q_i}{\partial x_i} + H_r + H_s + H_L, \quad (\text{S8})$$

with density ρ , flow velocity \mathbf{v} , deviatoric stress tensor σ' , pressure P , directional gravity \mathbf{g} , gravitational potential Φ , Newton's constant G , heat capacity c_P , temperature T , heat flux $q_i = -k \partial T / \partial x_i$, thermal conductivity k , and radiogenic (H_r), shear (H_s) and latent (H_L) heat production terms. Employing a Lagrangian marker-in-cell technique to integrate the energy equation, we minimise numerical diffusion and trace advection of non-diffusive flow properties during material deformation (Gerya 2019). The computational stencil is formulated using a fully staggered-grid finite-differences method, which captures sharp variations of stresses and thermal gradients in models with strongly variable viscosity and thermal conductivity.

The thermal disk gas boundary conditions of the planetesimals are assumed to be constant in time, $T_{\text{disk}} \equiv 150$ K. Radiogenic heating from ^{26}Al decays with time,

$$H_r(t) = f_{\text{Al}} \cdot \left(\frac{^{26}\text{Al}}{^{27}\text{Al}} \right)_{\text{CAI}} \cdot \frac{E_{^{26}\text{Al}}}{\tau_{^{26}\text{Al}}} \cdot e^{-\Delta t_{\text{CAI}} / \tau_{^{26}\text{Al}}}, \quad (\text{S9})$$

with the chondritic abundance of aluminum f_{Al} (Lodders 2003), the decay energy $E_{^{26}\text{Al}} = 3.12$ MeV (Castillo-Rogez et al. 2009), the time relative to CAI formation Δt_{CAI} , and the ^{26}Al mean lifetime $\tau_{^{26}\text{Al}} = 1.03$ Myr (Kita et al. 2013). The thermal consequences of magma ocean stages beyond the rock disaggregation threshold (Costa et al. 2009) are parameterized using a scaled thermal con-

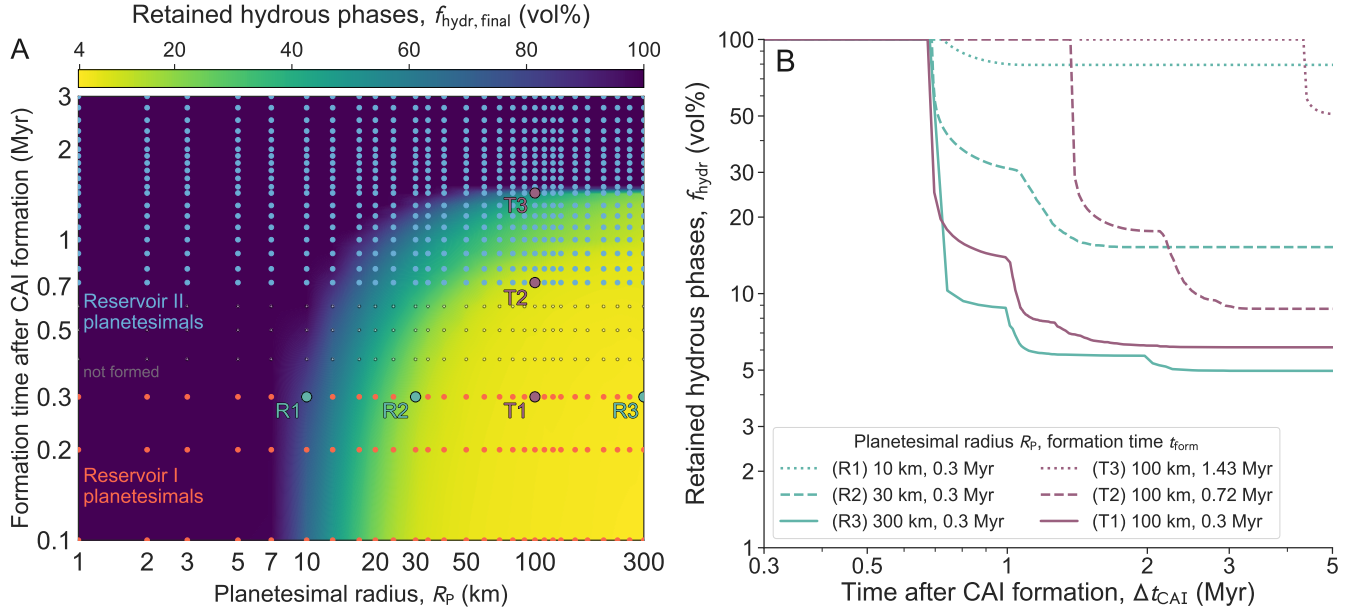


Figure S4. Parameter space and time evolution of retained hydrous rock phases in planetesimal simulations. (A) Analogous to Fig. 3A, but for the retained volumetric fraction of hydrous rock phases in simulated planetesimals after 5 Myr (thermochemical criterion $T < T_{\text{decomp}}$). Gray dots (labeled 'not formed') are used for the color interpolation, but do not contribute to Reservoir I or II. (B) Time evolution for distinct combinations of formation time and planetesimal radius. Lines R1–R3 and T1–T3 indicate the evolution of planetesimal simulations labeled in panel A.

ductivity,

$$k_{\text{eff}} = (q_{\text{conv}}/0.89)^{3/2} \cdot \alpha_{\text{liq}} g c_{\text{p-Si}} / (\Delta T^2 \rho_s \eta_{\text{num}}), \quad (\text{S10})$$

with the convective heat flux q_{conv} , the temperature difference across nodes ΔT , silicate density ρ_s , thermal expansivity of molten silicates α_{liq} , silicate heat capacity $c_{\text{p-Si}}$, local gravity $g(x, y)$, and lower cut-off viscosity η_{num} . Numerical rock properties and the I2ELVIS treatment of rock melting have been described previously (Lichtenberg et al. 2016).

To estimate the compositional evolution of planetesimals that form from an initial mixture of silicate rock, iron metal, and water ice, we follow an updated version of the procedure described in (Lichtenberg et al. 2019a; Monteux et al. 2018) and derive the fraction of each planetesimal in our simulation grid that exceed certain thermochemical criteria. We employ four criteria, two related to water ice melting and water-rock reactions, and two related to metal core formation. During radiogenic heat-up of a water-ice-rich planetesimal, the primordial ice melts and may react with the ambient rock to create hydrous silicates and oxidize available iron phases, resulting in loss of hydrogen to space (Castillo-Rogez & Young 2017; Sutton et al. 2017). While in liquid phase, the aqueous fluid may undergo pore water convection along a down-temperature gradient (Grimm & McSween 1993; Young et al. 1999), but a fraction of water can be trapped in hydrous silicate phases. Therefore, we derive approximate upper and lower ther-

mal bounds of the thermochemical interior evolution by calculating the fraction of the planetesimal body that exceeds certain threshold temperatures for ice melting/rock hydration at $T \geq T_{\text{hydr}} \equiv 273$ K, and dehydration and decomposition of the most stable hydrous silicate phases at $T \geq T_{\text{decomp}} \equiv 1223$ K (Monteux et al. 2018), which we regard as a generous upper limit, because most hydrous phases would be destroyed at much lower temperatures (Fu & Elkins-Tanton 2014; Nakamura 2006; Nakato et al. 2008). To estimate the fraction of the body that may undergo metal-silicate segregation, we employ two criteria. If substantial sulfur (S) is present in the parent body, an early, incomplete core may form (Bagdassarov et al. 2009) from an interconnected network of metal-sulfide phases in the host body and subsequent gravitational drainage (percolation) toward the center, which we fix to the Fe-FeS eutectic temperature at 1 bar, $T \geq T_{\text{perc}} \equiv 1273$ K. When temperatures rise further and silicate rocks start to melt they eventually reach the rock disaggregation threshold beyond a melt fraction of $\varphi \gtrsim 0.4$ (Costa et al. 2009), which is equivalent to ≈ 1639 K at 1 bar. Accordingly, at this melt fraction, $\varphi \geq \varphi_{\text{rain}} \equiv 0.4$, we assume closure of core formation due to efficient iron droplet rain-out from the internal magma ocean (Lichtenberg et al. 2018; Elkins-Tanton 2012; Patočka et al. 2020).

For each timestep in the disk evolution model we then compute the fraction $f_{\text{P,crit}}$ of computational markers in the planetesimal body that breach the aforementioned

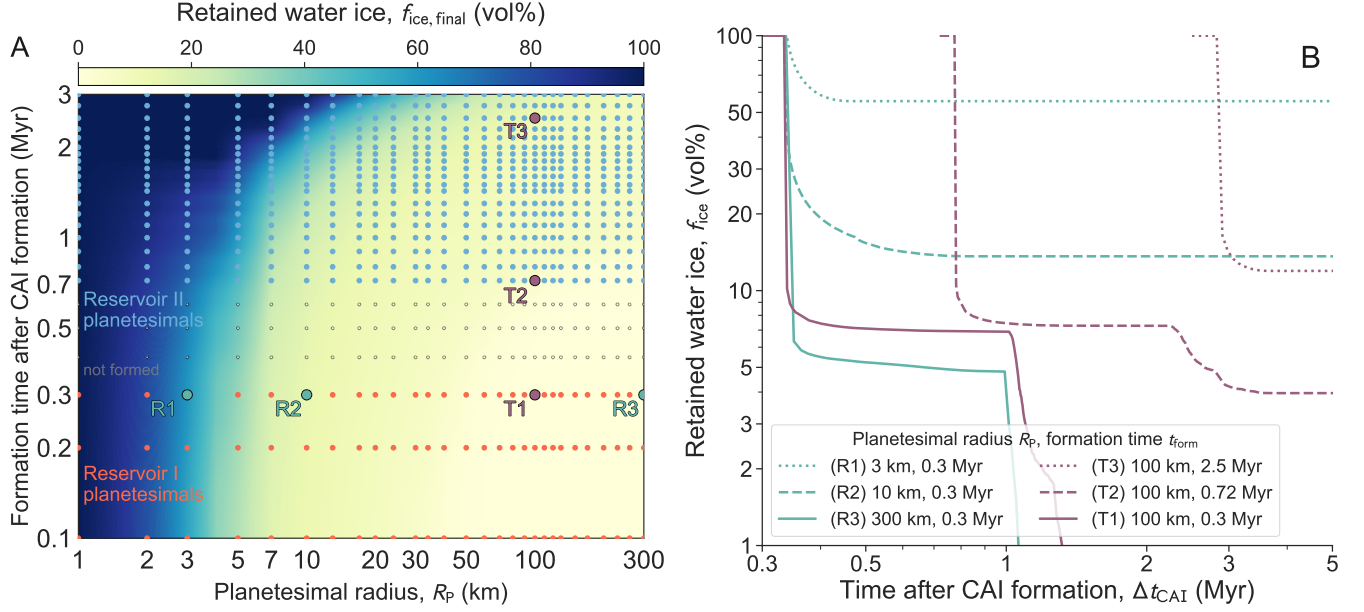


Figure S5. Parameter space and time evolution of retained water ice in planetesimal simulations. Same as Fig. S4, but for the retained volumetric fraction of water ice (thermochemical criterion $T < T_{hydr}$).

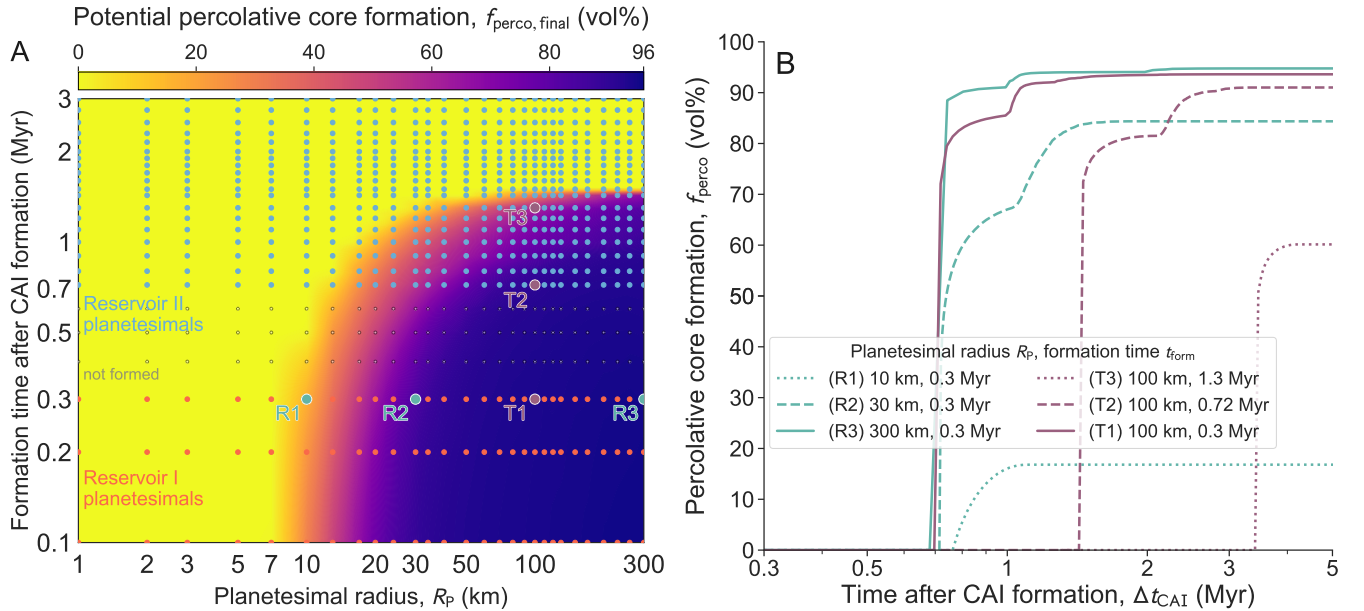


Figure S6. Parameter space and time evolution of core formation via metal percolation in planetesimal simulations. Same as Fig. S4, but for the volumetric fraction eligible for percolative core formation (thermochemical criterion $T \geq T_{perc}$).

thresholds,

$$f_{P,crit}(t) \equiv N_{\text{markers,crit}}/N_{\text{markers,total}}, \quad (\text{S11})$$

with $N_{\text{markers,crit}}$ the number of markers in a planetesimal that exceed the threshold, and $N_{\text{markers,total}}$ the total number of markers in the planetesimal body. Fig. 3A shows the peak temperatures for various combinations of planetesimal formation time and radius (as a volumetric mean per body); we show additional parameter ranges in Figs.

S4–S7. In general, larger planetesimal radius and earlier formation time (due to more live ^{26}Al) lead to higher temperatures in the interior. Peak temperatures are always reached at the center of the planetesimal, which is most insulated from the cold exterior. Typically, temperatures decrease from the inside out. However, because the penetration depth of inward conduction at the planetesimal surface is very limited (see below and Castillo-Rogez & Young (2017); Lichtenberg et al. (2016, 2019b)), plan-

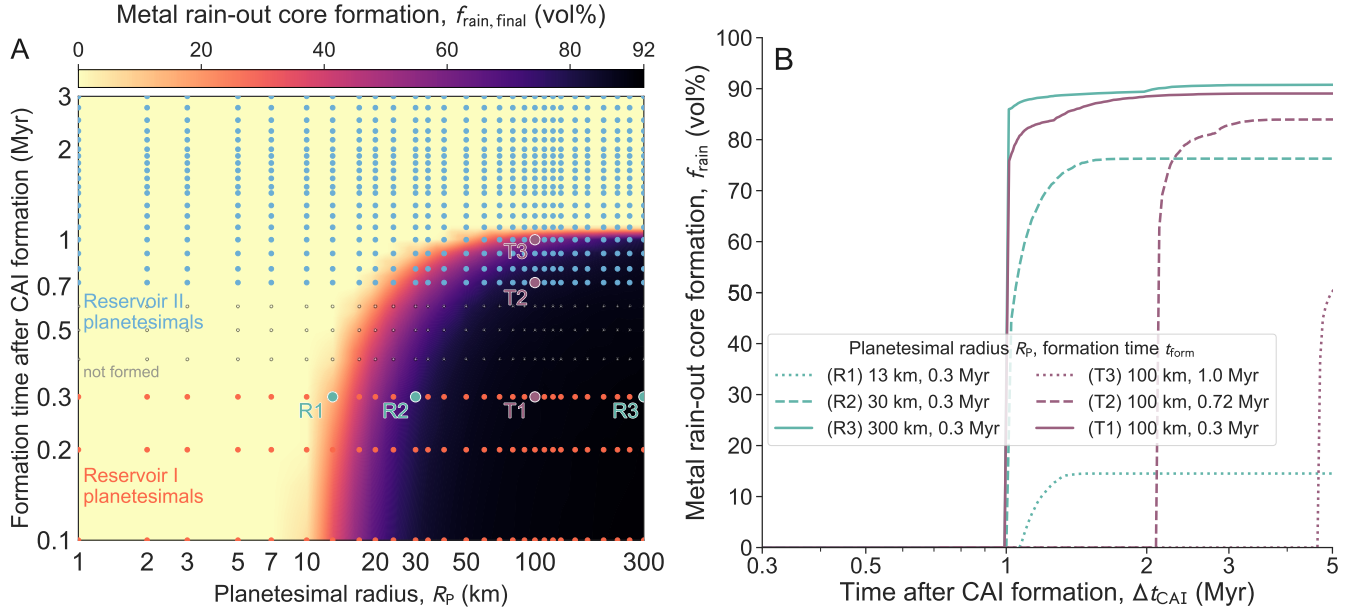


Figure S7. Parameter space and time evolution of core formation via metal rain-out in planetesimal simulations. Same as Fig. S4, but for the volumetric fraction eligible for rain-out core formation (thermochemical criterion $\varphi \geq \varphi_{\text{rain}}$).

etesimal interiors above ≈ 50 km in size are approximately isothermal in their deeper interiors after an initial heat-up phase. Once high silicate melt fractions beyond the disaggregation threshold are reached, the maximum temperatures are effectively buffered by convective heat transport.

The computational models cover the evolution of single planetesimals. To process the time-dependent evolution of the planetesimals formed in the disk simulation, we follow a procedure (Lichtenberg et al. 2018) to analyze the thermochemical evolution of a planetesimal population using a Monte Carlo approach that parameterizes the birth planetesimal population from the streaming instability mechanism, as indicated by fluid dynamical models (Johansen et al. 2015; Simon et al. 2017; Abod et al. 2019; Nesvorný et al. 2019). For each timestep in the planetesimal formation model (see above) we randomly generate a family of newly formed planetesimals that follow a radius power law

$$\frac{\partial N_{\text{P}}}{\partial R_{\text{P}}} \propto R_{\text{P}}^{-q}, \quad (\text{S12})$$

with the number of bodies in a specific radius bin N_{P} , and power law index $q = 2.8$ (Johansen et al. 2015; Simon et al. 2017), from which we generate integer radii $R_{\text{min}} \leq R_{\text{P}} \leq R_{\text{max}}$ according to

$$R_{\text{P}} = \lceil R_{\text{min}}(1 - x_{\text{rand}})^{-1/(q-1)} \rceil, \quad (\text{S13})$$

with pseudo-random number $x_{\text{rand}} \in [0, 1]$, approximating the total newly generated planetesimal mass per timestep and reservoir using

$$\frac{\partial M_{\text{P, res}}}{\partial t} = \int_{m_{\text{min}}}^{m_{\text{max}}} dm_{\text{P, res}}(R_{\text{P}}, t), \quad (\text{S14})$$

where the planetesimal mass m_{P} and the minimum and maximum bounds, m_{min} and m_{max} , are related to the planetesimal radius by a fixed initial mean density of $\rho_{\text{P}} = 2750 \text{ kg m}^{-3}$. We choose the minimum planetesimal radius in our parameter space to be $R_{\text{min}} = 1$ km, and set the upper bound of the birth planetesimal population to $R_{\text{max}} = 300$ km, consistent with a tapered power law toward larger planetesimal radii (Johansen et al. 2015; Abod et al. 2019) and planetesimal mean birth sizes on the order of ≈ 100 km (Morbidelli et al. 2009; Delbo et al. 2017).

To compute the compositional evolution of the whole planetesimal population per timestep and thermochemical criterion, we bin the planetesimal mass formed in the disk model into distinct radius bins according to the primordial planetesimal size-frequency distribution (Eq. S12). We then calculate the fraction of the planetesimal population per reservoir in a given radius and time bin that fulfills a specific thermochemical criterion as

$$f_{\text{pop, crit}}(t) = \frac{1}{N_{\text{P, tot}}(t)} \cdot \int_{R_{\text{min}}}^{R_{\text{max}}} N_{\text{P, bin}} \cdot f_{\text{bin, crit}} \cdot dV_{\text{bin}}(t), \quad (\text{S15})$$

with $N_{\text{P, tot}}(R_{\text{P}}, t)$ the total number of planetesimals per reservoir, $N_{\text{P, bin}}$ the number of planetesimals per bin, and $f_{\text{bin, crit}}(R_{\text{P}}, t) \cdot dV_{\text{bin}}(t)$ the volumetric fraction, linearly interpolated from the single planetesimal simulation grid described above. The volume change per timestep is normalized to the total planetesimal volume per reservoir and time after 5 Myr in the disk simulation. The volumetric fraction increases when more planetesimals form or when a

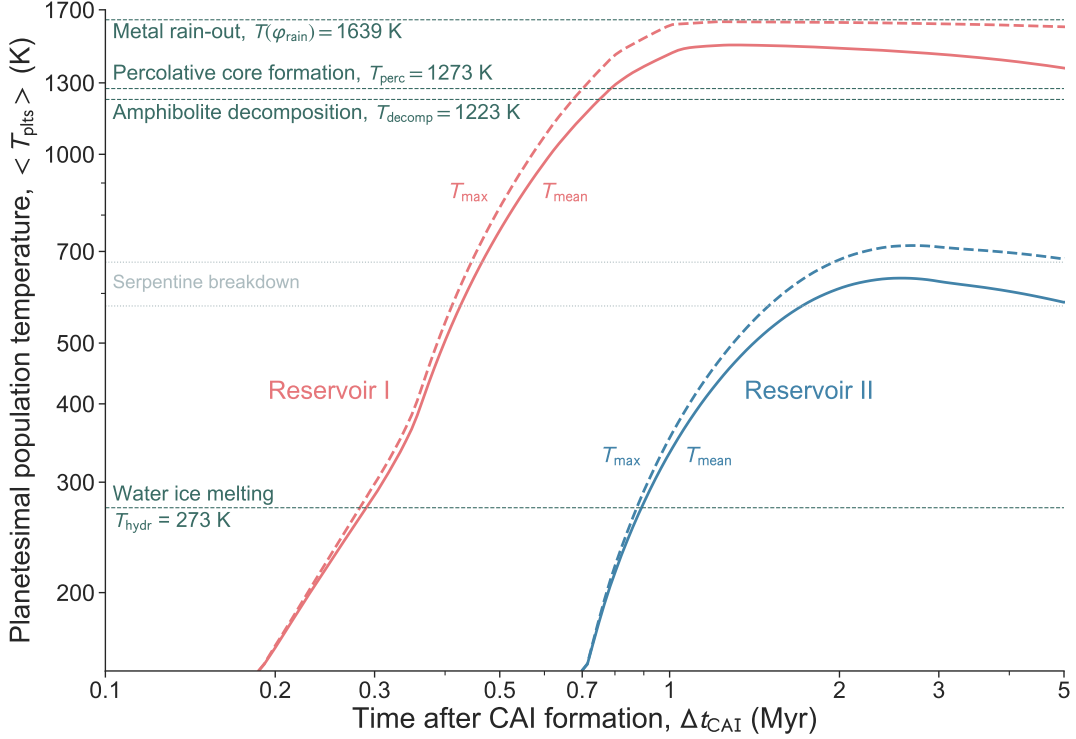


Figure S8. Temperature evolution of the simulated planetesimal populations. Shown are the evolution of the volumetric mean (solid lines) and maximum (dashed lines) temperatures over the whole planetesimal population. Reservoir I is indicated in red, Reservoir II in blue. Overplotted are the employed thermochemical criteria for the stability of water ice (T_{hydr}), hydrous rock (T_{decomp}), percolative core formation (T_{perc}), and rain-out core formation (φ_{rain}) with dark green dashed lines. Additionally we indicate the breakdown for more common serpentine phyllosilicate phases (gray dotted lines, labeled ‘Serpentine breakdown’) in the interval of $T \in [573\text{--}673]$ K (Nakamura 2006; Nakato et al. 2008).

planetesimal sub-volume starts to satisfy a specific criterion (e.g., hot enough for percolative core formation), and decreases when a planetesimal sub-volume does not satisfy a given criterion anymore (e.g., too hot for water ice stability). In Fig. S8 we display the combined temperature evolution of the planetesimal populations formed in the disk model in Reservoir I and Reservoir II together with the thermochemical criteria. The effects of minimum and maximum radii and choice of power law have been discussed elsewhere (Lichtenberg et al. 2018).

EXTERIOR HEATING EFFECTS ON PLANETESIMALS DUE TO DISK EVOLUTION

Our planetesimal models employ a constant temperature boundary condition, whereas in the disk simulations the local gas temperature can vary over time (Fig. S2). In general, the exterior disk temperature has minor effects on planetesimal evolution (Golabek et al. 2014). In this section we seek to determine whether it is negligible in our simulations. To estimate the effect of the time-dependent disk temperature on the thermal evolution of planetesimals, we developed a thermal diffusion code that solves the radial 1-D heat diffusion equation (Hevey & Sanders

2006; Gerya 2019),

$$\frac{\partial T}{\partial t} = \frac{k}{\rho c_p} \frac{1}{r^2} \frac{\partial}{\partial r} \left(r^2 \frac{\partial T}{\partial r} \right), \quad (\text{S16})$$

where T is the temperature, t is the time, k is the thermal conductivity, ρ is the density, c_p is the heat capacity and r is the radial distance from the center. We solve the heat diffusion equation using the implicit finite difference method (Gerya 2019). For consistency with the planetesimal calculations above, we assume that thermal conductivity, density and heat capacity are all temperature-independent and use the same values as employed in the more complex planetesimal models. As here we are only interested in the effect of the disk temperature on planetesimal evolution, we do not consider radiogenic heating. The initial temperature of the planetesimal interior is the same as in the previously described models.

To simulate the influence of the disk temperature on the planetesimal interior we prescribe the time-dependent disk temperature at 2 au as surface boundary condition, the orbital location with the highest temperatures where planetesimals form in the disk model (Fig. S9A). We model a profile across the entire planetesimal diameter over time, covering the various evolution stages of the disk. To check

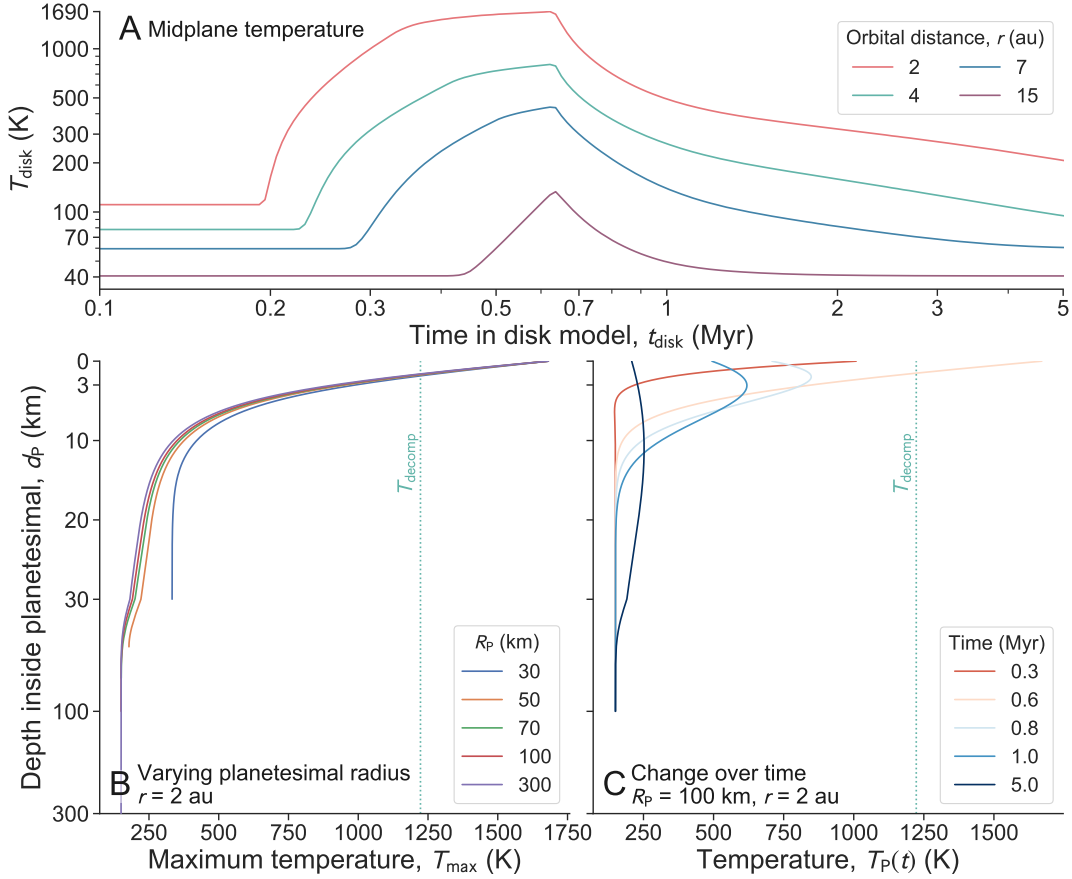


Figure S9. Effects of external disk temperature on the thermal profile in planetesimals. (A) Midplane gas temperature for 2, 4, 7, and 15 au in the disk simulation (lines). (B) Resulting peak temperature profiles in planetesimals between 30–300 km in radius at 2 au. The dashed green line shows the temperature criterion for hydrous rock decomposition (T_{decomp}). (C) Time evolution for a 100 km radius planetesimal at 2 au. Different line colors indicate different times during the disk lifetime.

numerical convergence of this simplified code, we performed calculations with different resolutions ranging from 1000 to 8000 grid points and tested timestep lengths ranging from 25 days to 1 yr. The results (Fig. S9) show the code has converged and demonstrate that disk heating of the planetesimals is limited to the near surface layers, thus only plays a volumetric role for small planetesimals, while the interiors of larger planetesimals remain mostly unaffected. Maximum temperatures achieved at various depths inside differently sized planetesimals are plotted in Fig. S9B and the time-evolution of temperature for the $R_p = 100$ km case is displayed in Fig. S9C. These are the maximum possible effects in the disk model. Internal temperatures of bodies formed at more distant orbits (Fig. S9A) are even less affected.

PLANETARY MIGRATION

To estimate the migration timescales for planetary embryos in Reservoir I and II (Fig. 1), we compute the torque from the disk on an embryo at each timestep and use this to evolve the total angular momentum of an embryo

of fixed mass with a first-order integrator. For type I migration (see e.g. Baruteau et al. (2014) for a review) the torque scales as

$$\Gamma_0 = \frac{q_P^2}{h^2} \Sigma_g r^4 \Omega_p^2, \quad (\text{S17})$$

with the embryo-to-star mass ratio $q_P = M_{\text{embryo}}/M_\star$, disk aspect ratio h , and Keplerian frequency Ω_p . The exact magnitude and direction of the torque can be written as a sum of the so-called Lindblad or ‘wave’ torque – generated by waves driven by the planet at resonant locations in the disk – and the corotation torque – generated by gas that is on average corotating with the planet. The wave torque (Paardekooper et al. 2010) can be written as

$$\gamma \Gamma_{\text{wave}}/\Gamma_0 = -2.5 - 1.7B + 0.1A, \quad (\text{S18})$$

where γ is the ratio of specific heats, B is the negative power law exponent of the local disk temperature profile and A is the negative power law exponent of the local disk density profile.

The calculation of the corotation torque requires determining how both diffusion within the gas and planetary

mass affect the material in this region. At a given viscosity, the torque peaks in magnitude as the non-linear ‘horseshoe drag’. With too little viscosity to replenish the angular momentum within this region, the horseshoe drag can become saturated, leaving only the Lindblad torque. For sufficiently high viscosity, the torque is forced into a linear regime which is reduced in magnitude. We therefore account for local disk conditions when computing the overall magnitude and direction of the torque. The linear and non-linear versions of the barotropic component of the torque (Paardekooper et al. 2010) are given by

$$\gamma\Gamma_{\text{lin,baro}}/\Gamma_0 = 0.7(3/2 - A), \quad (\text{S19})$$

$$\gamma\Gamma_{\text{hs,baro}}/\Gamma_0 = 1.1(3/2 - A) \quad (\text{S20})$$

respectively, while the entropy-related components of the linear corotation torque and horseshoe drag are given by

$$\gamma\Gamma_{\text{lin,ent}}/\Gamma_0 = (2.2 - 1.4/\gamma)\epsilon_e, \quad (\text{S21})$$

$$\gamma\Gamma_{\text{hs,ent}}/\Gamma_0 = 7.9\epsilon_e/\gamma, \quad (\text{S22})$$

respectively, with $\epsilon_e = B - (\gamma - 1)A$ being the negative of the local power law exponent of the specific entropy profile.

To choose γ , we utilise the fact that the temperature of the disk is set only by radiative and viscous heating, and radiative cooling. We expect the radiative processes to be much faster than the dynamical timescale, so consider the disk to be locally isothermal and use $\gamma = 1$. This assumption implicitly adds infinite thermal diffusion to the gas, driving the entropy-related part of the corotation torque into the linear regime. For transitioning between the unsaturated and saturated states of the torque, we simply switch various components of the corotation/horseshoe drag on and off as necessary – we consider the overall value of the torque Γ_{tot} to be defined by one of three regimes, largely governed by the behaviour of the barotropic component:

- ‘Unsaturated’, in which the total torque is the sum of the wave torque, the linear entropy-related torque and the non-linear barotropic horseshoe drag ($\Gamma_{\text{tot}} = \Gamma_{\text{wave}} + \Gamma_{\text{lin,ent}} + \Gamma_{\text{hs,baro}}$).
- ‘Saturated’, in which the corotation region is assumed to be totally depleted of angular momentum such that the planet feels no torque from this region and the only remaining component is the wave torque ($\Gamma_{\text{tot}} = \Gamma_{\text{wave}}$).
- ‘Linear’, in which the total torque is the sum of the wave torque and the linear forms of both the entropy-related and barotropic corotation torque ($\Gamma_{\text{tot}} = \Gamma_{\text{wave}} + \Gamma_{\text{lin,ent}} + \Gamma_{\text{lin,baro}}$).

We must then choose one of these three regimes at each timestep. The maximal, non-linear, unsaturated horseshoe drag is achieved when the disk viscosity parameter

α_v satisfies (Baruteau & Lin 2010)

$$0.16 \frac{q_p^{3/2}}{h^{7/2}} < \alpha_v < 0.16 \frac{q_p^{3/2}}{h^{9/2}}. \quad (\text{S23})$$

Values of α_v lower than the left-hand side of this criterion will cause the torque to become saturated, while values higher than the right-hand side will push the torque into its linear form. At each timestep we select a regime for the torque based on which of the inequalities in Eq. S23 is satisfied. We compute the total torque based on the regime and the value of Γ_0 , using Eq. S17 and the disk properties taken directly from the disk model. We linearly interpolate between different snapshots of this disk model to obtain values for disk properties on timescales relevant for migration. As a test of the validity of this model, we compared the estimated migration timescales with those in two hydrodynamical simulations of a migrating Earth-mass planet using the two-dimensional FARGO-3D code (Benítez-Llambay & Masset 2016). In both tests the planet started at 1.8 au with $\alpha_v = 1 \times 10^{-4}$, a surface density profile $\Sigma = (1000 \text{g/cm}^3)r^{-1}$ and $h \propto r^{1/4}$. We created these initial conditions in both model setups. In the first test we used $h = 0.073$ at 1 au, placing our model in the ‘linear’ regime. The difference between the migration rate in our model and the FARGO-3D simulations was around 7% over the 2000 yr simulation time. In the second test we used $h = 0.035$ (the ‘unsaturated’ regime) and found that the migration rate in the simulation was 32% faster than in our model. The parameters of the latter test would – according to the model in Paardekooper et al. (2011) – partially saturate the corotation torque in our disc. Because the corotation torque promotes outward migration in this disc, the partial saturation would result in faster migration in the hydrodynamical models as observed, so any difference between our model and equivalent hydrodynamical simulations is due to this approximate treatment of saturation. We conclude that a more sophisticated approach would not alter the conclusions of this paper.

In addition to the type I migration timescales we investigate whether a migrating protoplanet opens a gap in the disk, which may slow down its migration. To determine if and when this happens, we use the gap-opening criterion $P < 1$ (Crida et al. 2006), where

$$P = \frac{3^{4/3}}{4} \frac{h}{q_p^{1/3}} + \frac{50\alpha_v h^2}{q_p}. \quad (\text{S24})$$

We consider any embryo which satisfies $P < 1$ to be gap opening and calculate the threshold masses for each orbital radius and timestep to estimate whether a protoplanet in Reservoir II may be halted in its migration within the context of our disk model.

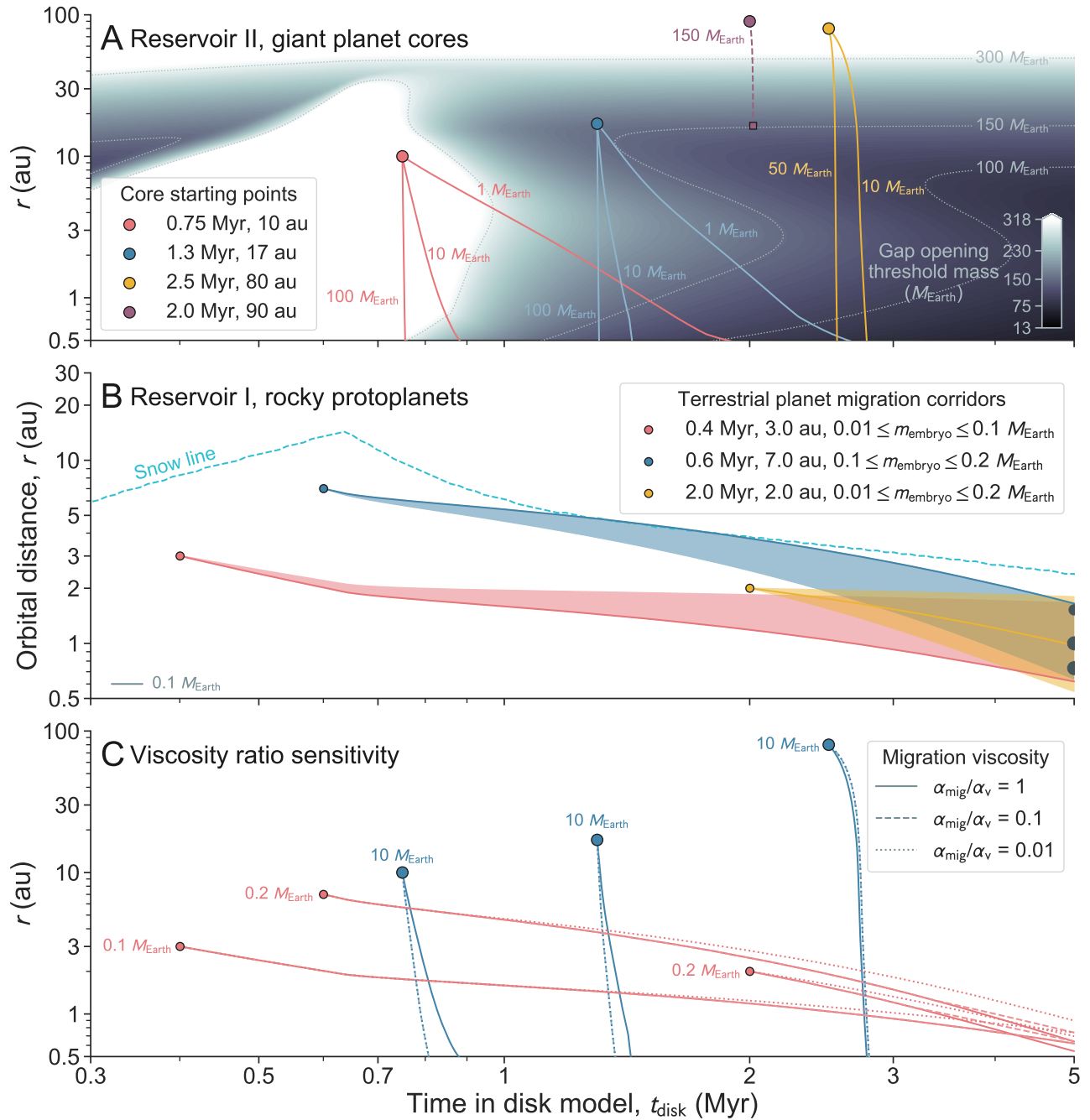


Figure S10. Type I and type II orbital migration in the disk simulation. (A) Migration of massive giant planet cores from starting locations and times (red, blue, yellow, and purple circles) located in Reservoir II. Lines show the migration path for a given mass (1, 10, 50, 100, or 150 Earth masses). The colored background indicates the mass threshold for a giant planet core to open a gap in the disk gas and transition from the type I to the type II migration regime (like the purple 150 M_{Earth} core). (B) Type I migration for various terrestrial planet embryo masses and starting locations and times (red, blue, and yellow circles) in Reservoir I. Lines and shades indicate the migration paths for a given starting location and protoplanet mass between 0.01–0.1 M_{Earth} (red), 0.1–0.2 M_{Earth} (blue), or 0.01–0.2 M_{Earth} (yellow). Planets that grow more massive during the disk lifetime would migrate inward of 0.5 au. (C) Disk viscosity sensitivity of the shown simulation tracks. For each starting location and time in Reservoir I (red circles) or II (blue circles), the disk viscosity that drives type I migration (α_{mig}) is varied between α_v (solid lines) and α_t (dotted lines).

Figs. 1 and S10 show migration tracks from this model. Fig. S10A shows the migration tracks of potentially early-formed giant planet cores in Reservoir II. In all but the 150 Earth mass (M_{Earth}) case, type I migration is too rapid to open up a gap and transition to the (slower) type II regime. In more comprehensive simulation setups, migration and growth show a complex interplay (Bitsch et al. 2019a,b; Johansen et al. 2019), but our models illustrate that early-formed giant planet cores typically migrate rapidly toward the star. Fig. S10B illustrates that also smaller-mass planets, such as the embryos that accrete to form the inner terrestrial planets, are limited in their maximum mass accretion during the disk phase. If they grow too fast and become too massive, they migrate rapidly inward. Later formation beyond the snow line (to reach the present-day orbits) would result in overly water-rich planets (Lichtenberg et al. 2019a; Bitsch et al. 2019b), inconsistent with the present-day volatile inventory of the Solar System terrestrial planets (Peslier et al. 2018). Fig. S10C displays the small sensitivity of the migration efficiency on the employed midplane viscosity. Whether protoplanets in the type I regime are migrating with α_v or α_t (see above) has little effect on the simulations.

Our model of migration is simplified by necessity and there are effects which cannot be accounted for in such a model that may affect the dynamical evolution of migrating protoplanets (Kley 2019), such as the heating torque (Benítez-Llambay et al. 2015; Bitsch et al. 2019b), variations in angular momentum transport in wind- or turbulence-driven disks (Kimmig et al. 2020), the interplay between growth and migration (Johansen et al. 2019), and dynamical interactions between multiple migrating embryos (Hands et al. 2014; Hands & Alexander 2018).

PLANETARY ACCRETION MODE

To determine the timescales for the onset of planetary accretion from an initially gravitationally collapsed population of planetesimals (Fig. 2), we employ theoretical prescriptions for planetesimal-planetesimal collisional growth (Ida & Lin 2004) and pebble accretion (Liu & Ormel 2018; Ormel & Liu 2018).

In the scenario of planetary growth via ballistic accretion of planetesimals (Safronov 1972; Morbidelli et al. 2012), the growth rate of the planetary embryos is determined by the velocity dispersion in the planetesimal population, which is equivalent to the eccentricity distribution. Eccentricity excitation is damped by gas drag, but less so for lower-mass planetesimals, which are excited by larger bodies. We use a previously-derived prescription for the growth timescale (i.e., the characteristic time for doubling the initial mass of a planetary object) in this scenario (Kokubo & Ida 2002). In this context, the growth time

scales as

$$\begin{aligned} \tau_{c,\text{acc}} \simeq & 1.2 \times 10^5 \left(\frac{\Sigma_d}{10 \text{ g cm}^{-2}} \right)^{-1} \left(\frac{r}{1 \text{ au}} \right)^{1/2} \\ & \times \left(\frac{M_{\text{embryo}}}{M_{\text{Earth}}} \right)^{1/3} \times \left(\frac{M_\star}{M_\odot} \right)^{-1/6} \\ & \times \left[\left(\frac{\Sigma_g}{2.4 \times 10^3 \text{ g cm}^{-2}} \right)^{-1/5} \right. \\ & \left. \times \left(\frac{r}{1 \text{ au}} \right)^{1/20} \times \left(\frac{m_P}{10^{18} \text{ g}} \right)^{1/15} \right]^2 \text{ yr}, \quad (\text{S25}) \end{aligned}$$

with the solid (dust) surface density Σ_d , semi-major axis r , mass of the accreting planetary embryo M_{embryo} , mass of the central star M_\star , mass of the Sun M_\odot , gas surface density Σ_g , and mass of the accreting low-mass planetesimals m_P . We determine the timescale for the onset of accretion from an initial planetesimal population produced from the streaming instability, which may be the bottleneck for the accretion of larger Mars-sized protoplanets within the disk lifetime (Visser & Ormel 2016; Liu et al. 2019). Following estimates of the initial mass function of planetesimals (IMF) (Johansen et al. 2015; Abod et al. 2019), we choose $M_{\text{embryo}} = 3.11 \times 10^{20} \text{ kg}$ and $m_P = 1.44 \times 10^{18} \text{ kg}$. Using mean densities of $\rho_P = 2750 \text{ kg m}^{-3}$, this translates to radii of $R_{\text{embryo}} = 300 \text{ km}$ and $R_P = 50 \text{ km}$, respectively. All other parameters for the growth timescale are calculated from the time-dependent evolution of the disk and dust coagulation model, as described above. Planetesimal growth becomes faster when more of the total mass is distributed in smaller objects, as they are more easily dynamically excited. In the chosen IMF, the majority of the planetesimal mass is in large objects, which we approximate by $R_P = 50 \text{ km}$. However, because of the $1/15$ -exponent in Eq. S25, the simulation results are only weakly affected by this choice. The timescale for the growth from pebble accretion (Ormel & Klahr 2010; Lambrechts & Johansen 2012) is estimated as (Liu & Ormel 2018; Ormel & Liu 2018)

$$\tau_{c,\text{PA}} = M_{\text{embryo}} / \left(\epsilon_{\text{PA}} \dot{M}_{\text{pebble}} \right), \quad (\text{S26})$$

with the pebble flux \dot{M}_{pebbles} and the pebble accretion efficiency

$$\epsilon_{\text{PA}} = f_{\text{set}} \epsilon_{\text{set}} + (1 - f_{\text{set}}) \epsilon_{\text{bal}}, \quad (\text{S27})$$

which approximates the effects of vertical turbulence on the dust particles in the ballistic and settling regimes of pebble accretion, depending on the settling fraction of individual pebbles f_{set} (Ormel & Liu 2018). The efficiencies

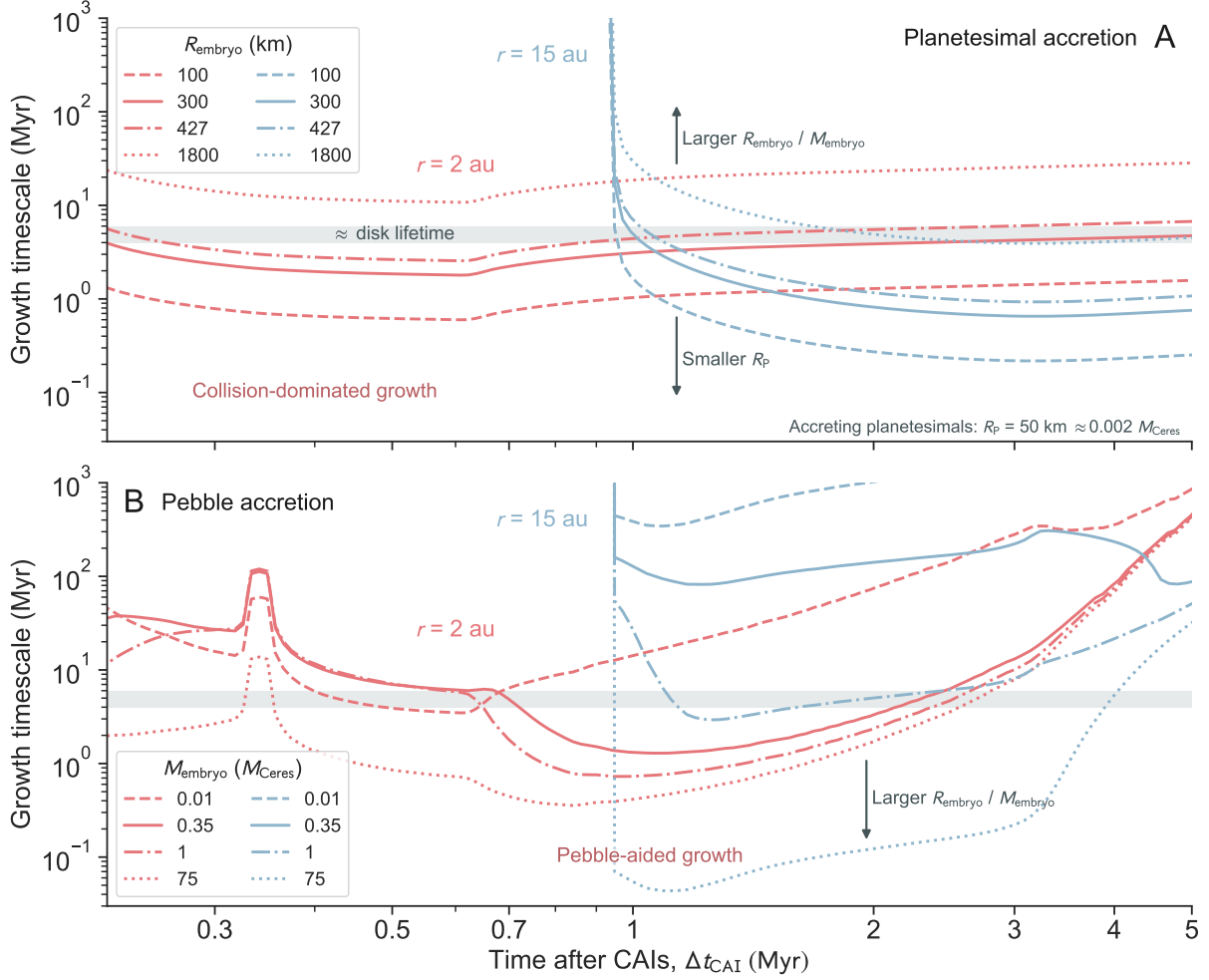


Figure S11. Growth timescale sensitivity for pebble and planetesimal accretion in Reservoir I and Reservoir II. The embryo radii and masses (legends) indicated in **A** and **B** are equivalent for constant planet density. **(A)** Growth timescale in the planetesimal (collision) accretion scenario for different embryo radii (dashed, solid, dash-dotted, and dotted lines). Red and blue indicate growth at 2 or 15 au, respectively. The gray horizontal band (labeled ‘ \approx disk lifetime’) indicates the approximate lifetime of the circum-solar disk. The up- and downward-pointing gray arrows indicate the trends for the growth timescale: increase for increasing embryo radius R_{embryo} , decrease for smaller planetesimals (R_p) that accrete onto the embryo. **(B)** Same as in panel **A**, but for pebble accretion. The growth timescale decreases for increasing protoplanet mass, but is highly sensitive to secular changes of the pebble flux in the disk simulation.

in the settling regime are given by

$$\epsilon_{\text{set}} = \left(\epsilon_{\text{set},2\text{D}}^{-2} + \epsilon_{\text{set},3\text{D}}^{-2} \right)^{-1/2}, \quad (\text{S28})$$

$$\epsilon_{\text{set},2\text{D}} = \frac{A_2}{\eta_{\text{disk}}} \sqrt{\frac{q_p \Delta v}{\tau_s v_K}} f_{\text{set}}, \quad (\text{S29})$$

$$\epsilon_{\text{set},3\text{D}} = A_3 \frac{q_p}{\eta_{\text{disk}} h_{\text{eff}}} f_{\text{set}}^2, \quad (\text{S30})$$

with the embryo-to-star mass ratio q_p , the disk radial pressure gradient η_{disk} , dimensionless stopping time τ_s , relative velocity between pebble and embryo Δv , Keplerian velocity

$$v_K = \sqrt{G(M_* + M_{\text{embryo}})/a}, \quad (\text{S31})$$

effective pebble disk aspect ratio h_{eff} , and numerical fit constants $A_2 = 0.32$ and $A_3 = 0.39$ (Ormel & Liu 2018).

The pebble accretion efficiencies in the ballistic regime are given by

$$\epsilon_{\text{bal},2\text{D}} = \frac{R_{\text{embryo}}}{2\pi\tau_s\eta_{\text{disk}}a} (1 - f_{\text{set}}) \times \sqrt{\frac{2q_p a}{R_{\text{embryo}}} + \left(\frac{\Delta v}{v_K}\right)^2}, \quad (\text{S32})$$

$$\epsilon_{\text{bal},3\text{D}} = \frac{1}{4\sqrt{2\pi}\eta_{\text{disk}}\tau_s h_P} (1 - f_{\text{set}}^2) \times \left(2q_p \frac{v_K}{\Delta v} \frac{R_{\text{embryo}}}{a} + \frac{R_{\text{embryo}}^2}{a^2} \frac{\Delta v}{v_K} \right), \quad (\text{S33})$$

with the pebble disk aspect ratio h_P (Liu & Ormel 2018). The direct dependence on the disk aspect ratio in the above formulation explains why pebble accretion in Fig. 2

is less efficient in the outer compared to the inner disk (Ormel & Liu 2018), which we discuss below. The pebble flux \dot{M}_{pebble} is derived from the disk and dust coagulation model (Drążkowska & Dullemond 2018). We assume that the growing embryos have no inclination. The pebble accretion efficiency ϵ_{PA} decreases with increasing inclination, so the pebble accretion timescale would be longer for an accreting embryo with non-zero inclination. As a compromise between the midplane and global viscosities (α_t and α_v , respectively) in the disk model, we choose a vertical diffusion of $\alpha_z = 1 \times 10^{-4}$ (cf. Ormel & Liu 2018).

Fig. S11 shows the sensitivity of the results in Fig. 2 to these parameter choices. In the collisional growth mode (Fig. S11A), larger protoplanet mass increases the growth timescale, which means slower growth. In contrast, in the pebble accretion mode, larger protoplanet mass decreases the growth timescale, which means faster growth. In the earliest disk stages, however, only for protoplanet masses substantially higher than the mass of Ceres (M_{Ceres} , $1 M_{\text{Ceres}} \approx 1.6 \times 10^{-4} M_{\text{Earth}}$) pebble accretion is faster than collisional accretion. Such high initial planetesimal masses are not produced in fluid dynamical simulations of the streaming instability mechanism (Johansen et al. 2015; Simon et al. 2016, 2017; Abod et al. 2019; Li et al. 2019; Rucska & Wadsley 2021), nor supported by asteroid belt size-frequency distribution reconstructions (Morbidelli et al. 2009; Delbo et al. 2017; Tsirvoulis et al. 2018), or the Kuiper-belt impact cratering record (Singer et al. 2019). In Reservoir I at around 1 Myr after CAI formation, if sufficiently massive embryos are present, the mass doubling timescale for pebble accretion onto Moon-like embryos is less than 1 Myr, which is the approximate time interval of a high pebble flux in the inner Solar System (cf. Fig. 2).

These results align with previous modeling results that suggest a heterogeneous transition of the dominant growth mode from collisional to pebble accretion (Johansen et al. 2015; Visser & Ormel 2016; Liu et al. 2019). In Reservoir II the growth timescales for pebble accretion display a larger deviation with embryo mass relative to Reservoir I, however, similarly initial growth must proceed via planetesimal collisions to reach masses susceptible for pebble accretion to commence. The increase in accretion timescale for Reservoir I starting at ≈ 3 Myr after CAI formation suggests that pebble accretion becomes inefficient even for higher masses at late disk stages. Previous simulations with a truncated pebble flux in the inner Solar System (Levison et al. 2015) and modeling work investigating super-Earth formation (Lambrechts et al. 2019b) similarly suggest a high sensitivity of protoplanet growth by pebble accretion on the local pebble flux.

OPEN SOURCE SOFTWARE PACKAGES

The numerical simulations and calculations in this work made use of SCIPY (Virtanen et al. 2020), NUMPY (Harris et al. 2020), PANDAS (McKinney 2010), and ASTROPY (Astropy Collaboration et al. 2018). Figures were produced using MATPLOTLIB (Hunter 2007) and SEABORN (Waskom & the seaborn development team 2020).

SUPPLEMENTARY TEXT

EVIDENCE FOR COMPOSITIONAL DICHOTOMY & ACCRETION CHRONOLOGY

There are compositional and mass budget trends with heliocentric distance (Hayashi 1981; Gradie & Tedesco 1982) for which various explanations have been proposed (Grimm & McSween 1993; Morbidelli et al. 2015, 2016). Mass budget calculations show $\approx 2M_{\text{Earth}}$ in solids in the inner and $\approx 445 M_{\text{Earth}} = 1.4 M_{\text{Jupiter}}$ in solids and gas in the outer Solar System planets (Morbidelli et al. 2015; Nimmo et al. 2018). Water abundance increases with orbital distance (DeMeo et al. 2015; Raymond et al. 2020). Hf-W dating of core segregation events (Kruijjer et al. 2014) and Pb-Pb ages of chondrules (Bollard et al. 2017) indicate that the planet-forming embryos of Earth and Mars started their accretion early during the disk phase at $\lesssim 1\text{--}2$ Myr after CAI formation, but did not gain their full mass until $\gtrsim 30$ Myr for Earth and $\approx 4\text{--}15$ Myr for Mars (Dauphas & Pourmand 2011; Rudge et al. 2010; Marchi et al. 2020), depending on the assumptions used in the Hf-W chronometry (Nimmo & Kleine 2007; Mezger et al. 2013).

A hypothesis for the origin of the observed CC/NC dichotomy is an early formation of Jupiter (Kruijjer et al. 2017; Desch et al. 2018; Scott et al. 2018), but the Hf-W constraints on the accretion process substantially narrow the possible parameter space for a simultaneous rapid accretion of proto-Jupiter (Alibert et al. 2018) and protracted growth of the inner terrestrial planets (Nimmo et al. 2018; Brasser & Mojzsis 2020). An alternative physical mechanism for the separation of the inner and outer Solar System reservoirs is required if proto-Jupiter formed far from the inner Solar System and late during the disk stage. This is consistent with Jupiter's atmospheric volatile budget (Öberg & Wordsworth 2019; Bosman et al. 2019) and the asymmetric distribution of its trojan asteroids (Pirani et al. 2019). The proposed filtering mechanism in the Jupiter barrier scenario is sensitive to the dynamical configuration of the gas giants (Haugbølle et al. 2019) and the dust destruction efficiency in the outer pressure bump (Drążkowska et al. 2019). It is also unclear by what mechanism gas accretion onto giant planets halts and if Jupiter would stop to grow at sufficient mass during the disk lifetime (Lambrechts et al. 2019a) if Jupiter's core would have been formed $\lesssim 1$ Myr after CAIs, as required for an early-

formed Jupiter to explain the CC/NC dichotomy (Kruijer et al. 2017).

The Hf-W time constraints on embryo growth indicate early core-segregation events on the parent bodies of iron meteorites in the inner Solar System reservoir from ≈ 0 –2 Myr after CAI formation (Kruijer et al. 2014, 2017; Hunt et al. 2018; Pape et al. 2019), which implies the formation of these bodies sometime earlier, contemporaneous with or shortly after the formation of CAIs (Connelly et al. 2012; Bouvier & Wadhwa 2010). In contrast, core segregation in the outer Solar System reservoir (as witnessed by carbonaceous chondrites or differentiated material related to it) is delayed relative to the inner Solar System by ≈ 1.3 Myr (Tab. S1). Astronomical observations of protoplanetary disks reveal a variety of substructure (Andrews et al. 2018), and indicate early grain growth during the disk infall stage (Harsono et al. 2018; Segura-Cox et al. 2020) and a decline of dust mass with time (Greaves & Rice 2010; Pascucci et al. 2016; Manara et al. 2018; Tychoniec et al. 2020). Some disks have been observed with ringed substructure as close in as ≈ 1 au (Andrews et al. 2016) or during the Class I disk stage (Segura-Cox et al. 2020). However, most observed disks are several Myr old, and the orbital locations of gaps (observed at mm wavelength) range from tens to hundreds of au. These disk observations complement the geochemical chronology and suggest the onset of planetary accretion potentially as early as the Class 0 or Class I disk stage of the Solar System (Pascucci & Tachibana 2010).

The formation of secondary minerals and the high oxidation state of iron phases in CC parent bodies reveal that they initially formed with larger water budgets and subsequently dehydrated (Grimm & McSween 1989; Alexander et al. 2018; Krot et al. 2015; Sutton et al. 2017). Inner Solar System water requires several sources (van Dishoeck et al. 2014; McCubbin & Barnes 2019; Peslier et al. 2018; Alexander et al. 2018). Similarities in noble gas abundances between carbonaceous chondrites and differentiated planetary bodies, and their nitrogen and hydrogen isotope ratios suggest CCs are the principal source of Earth's volatile elements (Alexander et al. 2012; Marty 2012), in addition to some potential nebular ingassing (Wu et al. 2018; Williams & Mukhopadhyay 2019). However, uncertainties persist in the timing of arrival of the volatile source bodies and their nature and prior internal evolution (Sarafian et al. 2014; Grewal et al. 2019; Sossi et al. 2019; Piani et al. 2020). Deuterium abundances indicate an early contribution from interstellar volatile ices (Cleeves et al. 2014; Piani et al. 2018) or extensive iron oxidation (Sutton et al. 2017). Estimates of the initial water abundance in meteoritic parent bodies range from several per cent (Marrocchi et al. 2018) to up to 50 per cent water by

Table S1. Times of metal-silicate segregation and aqueous alteration in meteorites. Times relative to CAI formation (Connelly et al. 2012). CM, CR, and CI values are weighted means from several meteorites (Doyle et al. 2015; Jilly-Rehak et al. 2017). Used to generate Figs. 4A and 5A. References: (1) Kruijer et al. (2017), (2) Hunt et al. (2018), (3) Doyle et al. (2015), (4) Fujiya et al. (2013), (5) Fujiya et al. (2012), (6) Jilly-Rehak et al. (2017).

Meteorite group	Reservoir	$\Delta t_{\text{CAI}} \pm 2\sigma$ (Myr)	Ref.
<i>Metal-silicate segregation</i>			
IC	NC	0.3 ± 0.5	(1)
IIAB	NC	0.8 ± 0.5	(1)
IIIAB	NC	1.2 ± 0.5	(1)
IVA	NC	1.5 ± 0.6	(1)
IIIE	NC	1.8 ± 0.7	(1)
IAB	NC	6.0 ± 0.8	(2)
IIIF	CC	2.2 ± 1.1	(1)
IID	CC	2.3 ± 0.6	(1)
IIF	CC	2.5 ± 0.7	(1)
IIC	CC	2.6 ± 1.3	(1)
IVB	CC	2.8 ± 0.7	(1)
<i>Aqueous alteration</i>			
OC	NC	$2.4^{+1.8}_{-1.3}$	(3)
Tagish Lake	CC	$4.1^{+1.3}_{-1.1}$	(4)
CM	CC	$4.1^{+0.5}_{-0.4}$	(5)
CV	CC	$4.2^{+0.8}_{-0.7}$	(3)
CR	CC	$4.2^{+1.8}_{-1.3}$	(6)
CI	CC	$4.4^{+0.6}_{-0.5}$	(4)
CO	CC	$5.1^{+0.5}_{-0.4}$	(3)

mass (Lodders 2003; van Dishoeck et al. 2014). Traces of fluid flow are widespread in the meteorite record, even in NC bodies (Lewis & Jones 2016; Lewis et al. 2018). The carbonaceous chondrites exhibit the widest range of water abundances (Alexander et al. 2012, 2018), but some NC chondrites also display substantial abundances with up to 6000 ppm H₂O (McCubbin & Barnes 2019). The range in measurements indicates that the delivery of water and other highly volatile elements to the inner terrestrial planets was subject to the stochastic and evolving nature of the accretion process.

NUCLEOSYNTHETIC ISOTOPE VARIABILITY IN PLANETARY MATERIALS

Distinct nucleosynthetic compositions have been identified for each meteorite parent body and planet, for which samples are available for analyses (i.e., Earth and Mars). These nucleosynthetic variations are caused by the heterogeneous distribution of presolar dust, carrying a char-

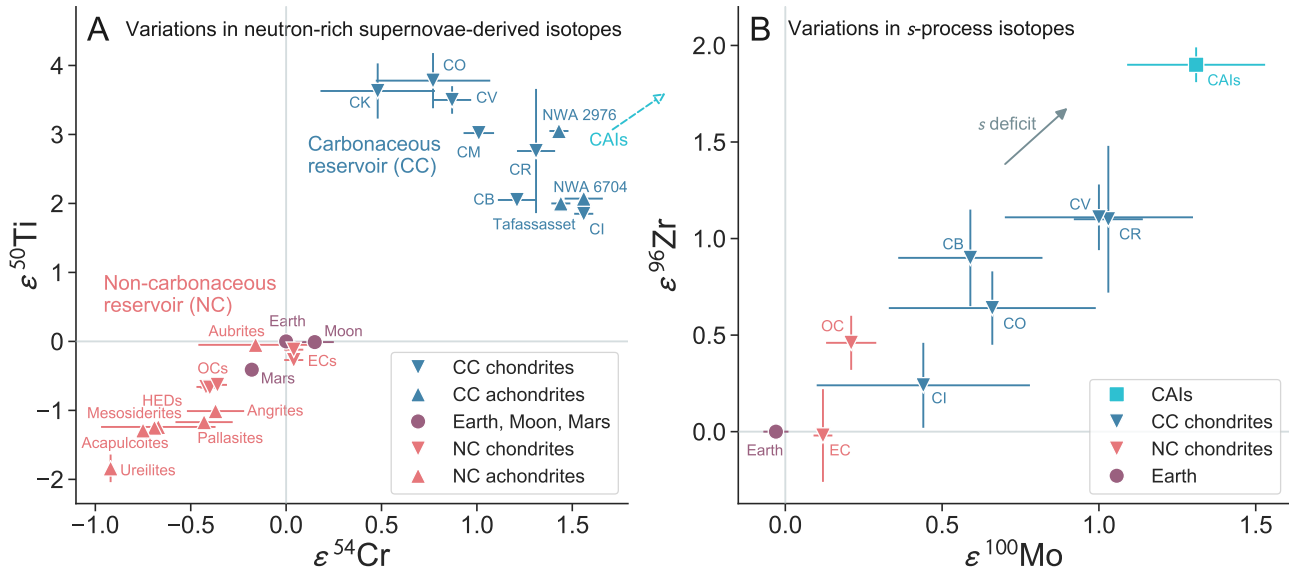


Figure S12. Nucleosynthetic isotope anomalies in Solar System planetary materials. (A) Nucleosynthetic Ti and Cr isotope data in ϵ notation (parts per 10,000 deviation of the ratio from the respective terrestrial standards). Average values are given for various chondrite and achondrite groups (symbols). Tafassasset, NWA 2976 and NWA 6704 refer to individual meteorites. Earth, Moon and Mars reflect data from Earth's mantle, lunar Apollo samples, and Martian meteorites for bulk compositions, respectively. HEDs (Howardite-Eucrite-Diogenites) are meteorites considered to originate from Vesta. CC = carbonaceous chondrites and related groups (blue), NC = non-carbonaceous groups (red), ECs = enstatite chondrites, OCS = ordinary chondrites. Data from (Trinquier et al. 2007; Leya et al. 2008, 2009; Larsen et al. 2011; Sanborn et al. 2019; Göpel et al. 2015). $2\text{-}\sigma$ uncertainties are indicated with red and blue lines on the symbols. The dashed turquoise arrow points toward the location of CAIs in Ti-Cr space, off the displayed axes limits. Light gray horizontal and vertical lines center on the axes origin. (B) Nucleosynthetic Zr and Mo isotope data of various chondrite classes. Same notation and colors as in panel A. Earth is most enriched in s -process isotopes compared to all other analyzed materials. Zr data from (Akram et al. 2013, 2015), Mo data from (Burkhardt et al. 2011; Render et al. 2018). Both panels adapted from Mezger et al. (2020).

acteristic isotopic composition that reflects its stellar formation site (Lugaro et al. 2018). This stardust contributed $\approx 3\%$ of the total dust in the protoplanetary disk (Hoppe et al. 2017). Stardust was incorporated to different extents into each planetary body and led to their distinct isotope compositions (Ek et al. 2019). Two first order types of anomalies can be distinguished (Fig. S12): variations in s -process isotopes (Ek et al. 2019; Render et al. 2018; Akram et al. 2015; Burkhardt et al. 2011) and variations in neutron-rich isotopes such as ^{48}Ca , ^{50}Ti and ^{54}Cr (Trinquier et al. 2007; Leya et al. 2008; Trinquier et al. 2009). The latter indicate nucleosynthesis in a supernova environment. The variability in neutron-rich isotopes shows a distinct difference between carbonaceous chondrites (CC) and the remaining Solar System material available for laboratory studies (i.e. non-carbonaceous chondrites, Mars and Earth, NC).

The origin of this isotopic dichotomy has broadly been attributed to two processes: (a) a change in composition of the material infalling onto the disk because of a heterogeneous distribution of stardust in the molecular cloud (Nanne et al. 2019; Jacquet et al. 2019) or (b) thermal processing and selective destruction of dust during the infall or in the disk itself. The latter process selectively removed

specific carrier phases of nucleosynthetic anomalies (Trinquier et al. 2009; Van Kooten et al. 2016) and assumes a homogeneous and well-mixed molecular cloud. In contrast to the neutron-rich nucleosynthetic variability (e.g., in ^{50}Ti or ^{54}Cr), the s -process variations show a single array with no clear dichotomy gap (Fig. S12B) (Akram et al. 2015; Ek et al. 2019), with the exception of Mo isotopes (Poole et al. 2017; Kruijer et al. 2017). Based on the s -process variations, dust grown in the interstellar medium (ISM) may have been destroyed by thermal processing leading to the s -process variations (Ek et al. 2019). This ISM-dust contributes $\approx 97\%$ of the dust in the protoplanetary disk (Hoppe et al. 2017) and has an average Solar System composition.

In our proposed scenario of early Solar System accretion (Fig. 6), a change in the composition of the infalling material (model (a)) can explain the initial establishment of the nucleosynthetic dichotomy (Nanne et al. 2019; Jacquet et al. 2019). Planetary objects in the Reservoir I region are dominated by material that is mainly fed to the inner disk during later infall stages and thus influences the composition of these planetesimals, while Reservoir II preferentially samples older material from before the infall changed composition. This older material, which includes

CAIs, is transported to the outer part of the disk during the Class I disk phase through viscous spreading and diffusional transport (Pignatale et al. 2018; Yang & Ciesla 2012; Nanne et al. 2019; Jacquet et al. 2019). However, in contrast to previous suggestions (Kruijer et al. 2017; Desch et al. 2018; Scott et al. 2018), our proposed scenario does not require the presence of proto-Jupiter to block the addition of outer Solar System materials to Reservoir I in the inner Solar System. Instead, both the chemical and isotopic dichotomy are an inherent consequence of the two subsequent episodes of planetesimal formation and the pebble flux suppression due to the dust pile-up along the drifting snow line.

Similarly, thermal processing of infalling dust (model (b)) is consistent with our proposed model and could have generated or contributed to the observed nucleosynthetic heterogeneities. However, selective destruction of dust in the disk itself is less likely, because in our model most of the thermal processing of inner Solar System material occurs inside of the planetesimals. This processing should not affect the nucleosynthetic anomalies because these are mainly carried by refractory elements (Toth et al. 2020).

REFERENCES

- Abod, C. P., Simon, J. B., Li, R., et al. 2019, *ApJ*, 883, 192, doi: [10.3847/1538-4357/ab40a3](https://doi.org/10.3847/1538-4357/ab40a3)
- Akram, W., Schönbachler, M., Bisterzo, S., & Gallino, R. 2015, *GeoCoA*, 165, 484, doi: [10.1016/j.gca.2015.02.013](https://doi.org/10.1016/j.gca.2015.02.013)
- Akram, W., Schönbachler, M., Sprung, P., & Vogel, N. 2013, *ApJ*, 777, 169, doi: [10.1088/0004-637X/777/2/169](https://doi.org/10.1088/0004-637X/777/2/169)
- Alexander, C. M. O., Bowden, R., Fogel, M. L., et al. 2012, *Science*, 337, 721, doi: [10.1126/science.1223474](https://doi.org/10.1126/science.1223474)
- Alexander, C. M. O., McKeegan, K. D., & Altwegg, K. 2018, *SSRv*, 214, 36, doi: [10.1007/s11214-018-0474-9](https://doi.org/10.1007/s11214-018-0474-9)
- Alibert, Y., Venturini, J., Helled, R., et al. 2018, *Nat. Astron.*, 2, 2397, doi: [10.1038/s41550-018-0557-2](https://doi.org/10.1038/s41550-018-0557-2)
- Andrews, S. M., Wilner, D. J., Zhu, Z., et al. 2016, *ApJL*, 820, L40, doi: [10.3847/2041-8205/820/2/L40](https://doi.org/10.3847/2041-8205/820/2/L40)
- Andrews, S. M., Huang, J., Pérez, L. M., et al. 2018, *ApJL*, 869, L41, doi: [10.3847/2041-8213/aaf741](https://doi.org/10.3847/2041-8213/aaf741)
- Ansdell, M., Williams, J. P., van der Marel, N., et al. 2016, *ApJ*, 828, 46, doi: [10.3847/0004-637X/828/1/46](https://doi.org/10.3847/0004-637X/828/1/46)
- Astropy Collaboration, Price-Whelan, A. M., Sipőcz, B. M., et al. 2018, *AJ*, 156, 123, doi: [10.3847/1538-3881/aabc4f](https://doi.org/10.3847/1538-3881/aabc4f)
- Aumatell, G., & Wurm, G. 2014, *MNRAS*, 437, 690, doi: [10.1093/mnras/stt1921](https://doi.org/10.1093/mnras/stt1921)
- Bagdassarov, N., Solferino, G., Golabek, G. J., & Schmidt, M. W. 2009, *Earth Planet. Sci. Lett.*, 288, 84, doi: [10.1016/j.epsl.2009.09.010](https://doi.org/10.1016/j.epsl.2009.09.010)
- Bai, X.-N. 2017, *ApJ*, 845, 75, doi: [10.3847/1538-4357/aa7dda](https://doi.org/10.3847/1538-4357/aa7dda)
- Bai, X.-N., Ye, J., Goodman, J., & Yuan, F. 2016, *ApJ*, 818, 152, doi: [10.3847/0004-637X/818/2/152](https://doi.org/10.3847/0004-637X/818/2/152)
- Balbus, S. A., & Hawley, J. F. 1991, *ApJ*, 376, 214, doi: [10.1086/170270](https://doi.org/10.1086/170270)
- Baruteau, C., & Lin, D. N. C. 2010, *ApJ*, 709, 759, doi: [10.1088/0004-637X/709/2/759](https://doi.org/10.1088/0004-637X/709/2/759)
- Baruteau, C., Crida, A., Paardekooper, S. J., et al. 2014, in *Protostars and Planets VI*, ed. H. Beuther, R. S. Klessen, C. P. Dullemond, & T. Henning, 667, doi: [10.2458/azu_uapress_9780816531240-ch029](https://doi.org/10.2458/azu_uapress_9780816531240-ch029)
- Benedikt, M. R., Scherf, M., Lammer, H., et al. 2020, *Icarus*, 347, 113772, doi: [10.1016/j.icarus.2020.113772](https://doi.org/10.1016/j.icarus.2020.113772)
- Benítez-Llambay, P., Masset, F., Koenigsberger, G., & Szulágyi, J. 2015, *Nature*, 520, 63, doi: [10.1038/nature14277](https://doi.org/10.1038/nature14277)
- Benítez-Llambay, P., & Masset, F. S. 2016, *ApJS*, 223, 11, doi: [10.3847/0067-0049/223/1/11](https://doi.org/10.3847/0067-0049/223/1/11)
- Birnstiel, T., Fang, M., & Johansen, A. 2016, *SSRv*, 205, 41, doi: [10.1007/s11214-016-0256-1](https://doi.org/10.1007/s11214-016-0256-1)
- Birnstiel, T., Klahr, H., & Ercolano, B. 2012, *A&A*, 539, A148, doi: [10.1051/0004-6361/201118136](https://doi.org/10.1051/0004-6361/201118136)
- Bitsch, B., Izidoro, A., Johansen, A., et al. 2019a, *A&A*, 623, A88, doi: [10.1051/0004-6361/201834489](https://doi.org/10.1051/0004-6361/201834489)
- Bitsch, B., Raymond, S. N., & Izidoro, A. 2019b, *A&A*, 624, A109, doi: [10.1051/0004-6361/201935007](https://doi.org/10.1051/0004-6361/201935007)
- Bollard, J., Connelly, J. N., Whitehouse, M. J., et al. 2017, *Sci. Adv.*, 3, e1700407, doi: [10.1126/sciadv.1700407](https://doi.org/10.1126/sciadv.1700407)
- Bosman, A. D., Cridland, A. J., & Miguel, Y. 2019, *A&A*, 632, L11, doi: [10.1051/0004-6361/201936827](https://doi.org/10.1051/0004-6361/201936827)
- Bouvier, A., & Wadhwa, M. 2010, *Nat. Geosci.*, 3, 637, doi: [10.1038/ngeo941](https://doi.org/10.1038/ngeo941)
- Brasser, R., & Mojzsis, S. J. 2020, *Nat. Astron.*, 4, 492, doi: [10.1038/s41550-019-0978-6](https://doi.org/10.1038/s41550-019-0978-6)
- Braukmüller, N., Wombacher, F., Funk, C., & Münker, C. 2019, *Nat. Geosci.*, 12, 564, doi: [10.1038/s41561-019-0375-x](https://doi.org/10.1038/s41561-019-0375-x)
- Burkhardt, C., Kleine, T., Oberli, F., et al. 2011, *Earth Planet. Sci. Lett.*, 312, 390, doi: [10.1016/j.epsl.2011.10.010](https://doi.org/10.1016/j.epsl.2011.10.010)
- Carrera, D., Gorti, U., Johansen, A., & Davies, M. B. 2017, *ApJ*, 839, 16, doi: [10.3847/1538-4357/aa6932](https://doi.org/10.3847/1538-4357/aa6932)
- Castillo-Rogez, J., Johnson, T. V., Lee, M. H., et al. 2009, *Icarus*, 204, 658, doi: [10.1016/j.icarus.2009.07.025](https://doi.org/10.1016/j.icarus.2009.07.025)

- Castillo-Rogez, J., & Young, E. D. 2017, in *Planetesimals: Early Differentiation and Consequences for Planets*, ed. L. T. Elkins-Tanton & B. P. Weiss (Cambridge: Cambridge University Press), 92–114
- Charnoz, S., Pignatale, F. C., Hyodo, R., et al. 2019, *A&A*, 627, A50, doi: [10.1051/0004-6361/201833216](https://doi.org/10.1051/0004-6361/201833216)
- Ciesla, F. J., & Cuzzi, J. N. 2006, *Icarus*, 181, 178, doi: [10.1016/j.icarus.2005.11.009](https://doi.org/10.1016/j.icarus.2005.11.009)
- Cleeves, L. I., Bergin, E. A., Alexander, C. M. O. D., et al. 2014, *Science*, 345, 1590, doi: [10.1126/science.1258055](https://doi.org/10.1126/science.1258055)
- Connelly, J. N., Bizzarro, M., Krot, A. N., et al. 2012, *Science*, 338, 651, doi: [10.1126/science.1226919](https://doi.org/10.1126/science.1226919)
- Costa, A., Caricchi, L., & Bagdassarov, N. 2009, *Geochem. Geophys. Geosys.*, 10, Q03010, doi: [10.1029/2008GC002138](https://doi.org/10.1029/2008GC002138)
- Crida, A., Morbidelli, A., & Masset, F. 2006, *Icarus*, 181, 587, doi: [10.1016/j.icarus.2005.10.007](https://doi.org/10.1016/j.icarus.2005.10.007)
- Cuzzi, J. N., & Zahnle, K. J. 2004, *ApJ*, 614, 490, doi: [10.1086/423611](https://doi.org/10.1086/423611)
- Dauphas, N., & Pourmand, A. 2011, *Nature*, 473, 489, doi: [10.1038/nature10077](https://doi.org/10.1038/nature10077)
- Davidson, J., Busemann, H., Nittler, L. R., et al. 2014, *GeoCoA*, 139, 248, doi: [10.1016/j.gca.2014.04.026](https://doi.org/10.1016/j.gca.2014.04.026)
- Delbo, M., Walsh, K., Bolin, B., Avdellidou, C., & Morbidelli, A. 2017, *Science*, 357, 1026, doi: [10.1126/science.aam6036](https://doi.org/10.1126/science.aam6036)
- DeMeo, F. E., Alexander, C. M. O., Walsh, K. J., Chapman, C. R., & Binzel, R. P. 2015, in *Asteroids IV*, University of Arizona Press, Tucson, ed. P. Michel, F. E. DeMeo, & W. F. Bottke, 13–41, doi: [10.2458/azu_uapress_9780816532131-ch002](https://doi.org/10.2458/azu_uapress_9780816532131-ch002)
- Desch, S. J., Kalyaan, A., & O'D. Alexander, C. M. 2018, *ApJS*, 238, 11, doi: [10.3847/1538-4365/aad95f](https://doi.org/10.3847/1538-4365/aad95f)
- Doyle, P. M., Jogo, K., Nagashima, K., et al. 2015, *Nat. Commun.*, 6, 7444, doi: [10.1038/ncomms8444](https://doi.org/10.1038/ncomms8444)
- Drążkowska, J., & Alibert, Y. 2017, *A&A*, 608, A92, doi: [10.1051/0004-6361/201731491](https://doi.org/10.1051/0004-6361/201731491)
- Drążkowska, J., & Dullemond, C. P. 2018, *A&A*, 614, A62, doi: [10.1051/0004-6361/201732221](https://doi.org/10.1051/0004-6361/201732221)
- Drążkowska, J., Li, S., Birnstiel, T., Stammler, S. M., & Li, H. 2019, *ApJ*, 885, 91, doi: [10.3847/1538-4357/ab46b7](https://doi.org/10.3847/1538-4357/ab46b7)
- Drążkowska, J., Alibert, Y., & Moore, B. 2016, *A&A*, 594, A105, doi: [10.1051/0004-6361/201628983](https://doi.org/10.1051/0004-6361/201628983)
- Dullemond, C. P., Apai, D., & Walch, S. 2006a, *ApJL*, 640, L67, doi: [10.1086/503100](https://doi.org/10.1086/503100)
- Dullemond, C. P., Natta, A., & Testi, L. 2006b, *ApJL*, 645, L69, doi: [10.1086/505744](https://doi.org/10.1086/505744)
- Ek, M., Hunt, A. C., Lugaro, M., & Schönstäbcher, M. 2019, *Nat. Astron.*, 4, 273, doi: [10.1038/s41550-019-0948-z](https://doi.org/10.1038/s41550-019-0948-z)
- Elkins-Tanton, L. T. 2012, *Annu. Rev. Earth Planet. Sci.*, 40, 113, doi: [10.1146/annurev-earth-042711-105503](https://doi.org/10.1146/annurev-earth-042711-105503)
- Ercolano, B., Jennings, J., Rosotti, G., & Birnstiel, T. 2017, *MNRAS*, 472, 4117, doi: [10.1093/mnras/stx2294](https://doi.org/10.1093/mnras/stx2294)
- Ercolano, B., & Pascucci, I. 2017, *R. Soc. Open Sci.*, 4, 170114, doi: [10.1098/rsos.170114](https://doi.org/10.1098/rsos.170114)
- Ferrière, K. M. 2001, *Rev. Mod. Phys.*, 73, 1031, doi: [10.1103/RevModPhys.73.1031](https://doi.org/10.1103/RevModPhys.73.1031)
- Flaherty, K., Hughes, A. M., Simon, J. B., et al. 2020, *ApJ*, 895, 109, doi: [10.3847/1538-4357/ab8cc5](https://doi.org/10.3847/1538-4357/ab8cc5)
- Flaherty, K. M., Hughes, A. M., Rosenfeld, K. A., et al. 2015, *ApJ*, 813, 99, doi: [10.1088/0004-637X/813/2/99](https://doi.org/10.1088/0004-637X/813/2/99)
- Flaherty, K. M., Hughes, A. M., Rose, S. C., et al. 2017, *ApJ*, 843, 150, doi: [10.3847/1538-4357/aa79f9](https://doi.org/10.3847/1538-4357/aa79f9)
- Flock, M., Fromang, S., González, M., & Commerçon, B. 2013, *A&A*, 560, A43, doi: [10.1051/0004-6361/201322451](https://doi.org/10.1051/0004-6361/201322451)
- Fu, R. R., & Elkins-Tanton, L. T. 2014, *Earth Planet. Sci. Lett.*, 390, 128, doi: [10.1016/j.epsl.2013.12.047](https://doi.org/10.1016/j.epsl.2013.12.047)
- Fujiya, W., Sugiura, N., Hotta, H., Ichimura, K., & Sano, Y. 2012, *Nat. Commun.*, 3, 627, doi: [10.1038/ncomms1635](https://doi.org/10.1038/ncomms1635)
- Fujiya, W., Sugiura, N., Sano, Y., & Hiyagon, H. 2013, *Earth Planet. Sci. Lett.*, 362, 130, doi: [10.1016/j.epsl.2012.11.057](https://doi.org/10.1016/j.epsl.2012.11.057)
- Gammie, C. F. 1996, *ApJ*, 457, 355, doi: [10.1086/176735](https://doi.org/10.1086/176735)
- Gerya, T. V. 2019, *Introduction to numerical geodynamic modelling* (Cambridge University Press)
- Gerya, T. V., & Yuen, D. A. 2003, *Phys. Earth Planet. Inter.*, 140, 293, doi: [10.1016/j.pepi.2003.09.006](https://doi.org/10.1016/j.pepi.2003.09.006)
- . 2007, *Phys. Earth Planet. Inter.*, 163, 83, doi: [10.1016/j.pepi.2007.04.015](https://doi.org/10.1016/j.pepi.2007.04.015)
- Golabek, G. J., Bourdon, B., & Gerya, T. V. 2014, *M&PS*, 49, 1083, doi: [10.1111/maps.12302](https://doi.org/10.1111/maps.12302)
- Göpel, C., Birck, J.-L., Galy, A., Barrat, J.-A., & Zanda, B. 2015, *GeoCoA*, 156, 1, doi: [10.1016/j.gca.2015.02.008](https://doi.org/10.1016/j.gca.2015.02.008)
- Gradie, J., & Tedesco, E. 1982, *Science*, 216, 1405, doi: [10.1126/science.216.4553.1405](https://doi.org/10.1126/science.216.4553.1405)
- Greaves, J. S., & Rice, W. K. M. 2010, *MNRAS*, 407, 1981, doi: [10.1111/j.1365-2966.2010.17043.x](https://doi.org/10.1111/j.1365-2966.2010.17043.x)
- Grewal, D. S., Dasgupta, R., Sun, C., Tsuno, K., & Costin, G. 2019, *Sci. Adv.*, 5, eaau3669, doi: [10.1126/sciadv.aau3669](https://doi.org/10.1126/sciadv.aau3669)
- Grimm, R. E., & McSween, H. Y. 1993, *Science*, 259, 653
- Grimm, R. E., & McSween, Jr., H. Y. 1989, *Icarus*, 82, 244, doi: [10.1016/0019-1035\(89\)90038-9](https://doi.org/10.1016/0019-1035(89)90038-9)
- Hands, T. O., & Alexander, R. D. 2018, *MNRAS*, 474, 3998, doi: [10.1093/mnras/stx2711](https://doi.org/10.1093/mnras/stx2711)
- Hands, T. O., Alexander, R. D., & Dehnen, W. 2014, *MNRAS*, 445, 749, doi: [10.1093/mnras/stu1751](https://doi.org/10.1093/mnras/stu1751)
- Harris, C. R., Millman, K. J., van der Walt, S. J., et al. 2020, *Nature*, 585, 357–362, doi: [10.1038/s41586-020-2649-2](https://doi.org/10.1038/s41586-020-2649-2)
- Harsono, D., Bjerkeli, P., van der Wiel, M. H. D., et al. 2018, *Nat. Astron.*, 2, 646, doi: [10.1038/s41550-018-0497-x](https://doi.org/10.1038/s41550-018-0497-x)
- Haugbølle, T., Weber, P., Wielandt, D. P., et al. 2019, *AJ*, 158, 55, doi: [10.3847/1538-3881/ab1591](https://doi.org/10.3847/1538-3881/ab1591)

- Hayashi, C. 1981, *Progress of Theoretical Physics Supplement*, 70, 35, doi: [10.1143/PTPS.70.35](https://doi.org/10.1143/PTPS.70.35)
- Hevey, P. J., & Sanders, I. S. 2006, *Meteorit. Planet. Sci.*, 41, 95, doi: [10.1111/j.1945-5100.2006.tb00195.x](https://doi.org/10.1111/j.1945-5100.2006.tb00195.x)
- Hin, R. C., Coath, C. D., Carter, P. J., et al. 2017, *Nature*, 549, 511, doi: [10.1038/nature23899](https://doi.org/10.1038/nature23899)
- Hoppe, P., Leitner, J., & Kodolányi, J. 2017, *Nat. Astron.*, 1, 617, doi: [10.1038/s41550-017-0215-0](https://doi.org/10.1038/s41550-017-0215-0)
- Hueso, R., & Guillot, T. 2005, *A&A*, 442, 703, doi: [10.1051/0004-6361:20041905](https://doi.org/10.1051/0004-6361:20041905)
- Hunt, A. C., Cook, D. L., Lichtenberg, T., et al. 2018, *Earth Planet. Sci. Lett.*, 482, 490, doi: [10.1016/j.epsl.2017.11.034](https://doi.org/10.1016/j.epsl.2017.11.034)
- Hunter, J. D. 2007, *Comput. Sci. Eng.*, 9, 90
- Ida, S., & Guillot, T. 2016, *A&A*, 596, L3, doi: [10.1051/0004-6361/201629680](https://doi.org/10.1051/0004-6361/201629680)
- Ida, S., & Lin, D. N. C. 2004, *ApJ*, 616, 567, doi: [10.1086/424830](https://doi.org/10.1086/424830)
- Ida, S., Yamamura, T., & Okuzumi, S. 2019, *A&A*, 624, A28, doi: [10.1051/0004-6361/201834556](https://doi.org/10.1051/0004-6361/201834556)
- Jacquet, E., Pignatale, F. C., Chaussidon, M., & Charnoz, S. 2019, *ApJ*, 884, 32, doi: [10.3847/1538-4357/ab38c1](https://doi.org/10.3847/1538-4357/ab38c1)
- Jilly-Rehak, C. E., Huss, G. R., & Nagashima, K. 2017, *GeoCoA*, 201, 224, doi: [10.1016/j.gca.2016.08.033](https://doi.org/10.1016/j.gca.2016.08.033)
- Johansen, A., Blum, J., Tanaka, H., et al. 2014, in *Protostars and Planets VI*, ed. H. Beuther, R. S. Klessen, C. P. Dullemond, & T. Henning, 547, doi: [10.2458/azu_uapress_9780816531240-ch024](https://doi.org/10.2458/azu_uapress_9780816531240-ch024)
- Johansen, A., Ida, S., & Brasser, R. 2019, *A&A*, 622, A202, doi: [10.1051/0004-6361/201834071](https://doi.org/10.1051/0004-6361/201834071)
- Johansen, A., Mac Low, M.-M., Lacerda, P., & Bizzarro, M. 2015, *Sci. Adv.*, 1, e1500109, doi: [10.1126/sciadv.1500109](https://doi.org/10.1126/sciadv.1500109)
- Johansen, A., Oishi, J. S., Mac Low, M.-M., et al. 2007, *Nature*, 448, 1022, doi: [10.1038/nature06086](https://doi.org/10.1038/nature06086)
- Kimmig, C. N., Dullemond, C. P., & Kley, W. 2020, *A&A*, 633, A4, doi: [10.1051/0004-6361/201936412](https://doi.org/10.1051/0004-6361/201936412)
- Kita, N. T., Yin, Q.-Z., MacPherson, G. J., et al. 2013, *Meteorit. Planet. Sci.*, 48, 1383, doi: [10.1111/maps.12141](https://doi.org/10.1111/maps.12141)
- Kley, W. 2019, in *Saas-Fee Advanced Course 45: From Protoplanetary Disks to Planet Formation* (Springer), 151
- Kokubo, E., & Ida, S. 2002, *ApJ*, 581, 666, doi: [10.1086/344105](https://doi.org/10.1086/344105)
- Krot, A. N., Nagashima, K., Alexander, C. M. O., et al. 2015, in *Asteroids IV*, ed. P. Michel, F. E. DeMeo, & W. F. Bottke, 635–660, doi: [10.2458/azu_uapress_9780816532131-ch033](https://doi.org/10.2458/azu_uapress_9780816532131-ch033)
- Kruijer, T. S., Burkhardt, C., Budde, G., & Kleine, T. 2017, *Proc. Natl. Acad. Sci. U.S.A.*, 114, 6712, doi: [10.1073/pnas.1704461114](https://doi.org/10.1073/pnas.1704461114)
- Kruijer, T. S., Touboul, M., Fischer-Gödde, M., et al. 2014, *Science*, 344, 1150, doi: [10.1126/science.1251766](https://doi.org/10.1126/science.1251766)
- Lambrechts, M., & Johansen, A. 2012, *A&A*, 544, A32, doi: [10.1051/0004-6361/201219127](https://doi.org/10.1051/0004-6361/201219127)
- Lambrechts, M., Lega, E., Nelson, R. P., Crida, A., & Morbidelli, A. 2019a, *A&A*, 630, A82, doi: [10.1051/0004-6361/201834413](https://doi.org/10.1051/0004-6361/201834413)
- Lambrechts, M., Morbidelli, A., Jacobson, S. A., et al. 2019b, *A&A*, 627, A83, doi: [10.1051/0004-6361/201834229](https://doi.org/10.1051/0004-6361/201834229)
- Larsen, K. K., Trinquier, A., Paton, C., et al. 2011, *ApJL*, 735, L37, doi: [10.1088/2041-8205/735/2/L37](https://doi.org/10.1088/2041-8205/735/2/L37)
- Lesur, G., Kunz, M. W., & Fromang, S. 2014, *A&A*, 566, A56, doi: [10.1051/0004-6361/201423660](https://doi.org/10.1051/0004-6361/201423660)
- Levison, H. F., Kretke, K. A., Walsh, K. J., & Bottke, W. F. 2015, *Proc. Natl. Acad. Sci. U.S.A.*, 112, 14180, doi: [10.1073/pnas.1513364112](https://doi.org/10.1073/pnas.1513364112)
- Lewis, J. A., & Jones, R. H. 2016, *Meteorit. Planet. Sci.*, 51, 1886, doi: [10.1111/maps.12719](https://doi.org/10.1111/maps.12719)
- Lewis, J. A., Jones, R. H., & Garcea, S. C. 2018, *GeoCoA*, 240, 293, doi: [10.1016/j.gca.2018.08.002](https://doi.org/10.1016/j.gca.2018.08.002)
- Leya, I., Schönbächler, M., Krähenbühl, U., & Halliday, A. N. 2009, *ApJ*, 702, 1118, doi: [10.1088/0004-637X/702/2/1118](https://doi.org/10.1088/0004-637X/702/2/1118)
- Leya, I., Schönbächler, M., Wiechert, U., Krähenbühl, U., & Halliday, A. N. 2008, *Earth Planet. Sci. Lett.*, 266, 233, doi: [10.1016/j.epsl.2007.10.017](https://doi.org/10.1016/j.epsl.2007.10.017)
- Li, R., Youdin, A. N., & Simon, J. B. 2019, *ApJ*, 885, 69, doi: [10.3847/1538-4357/ab480d](https://doi.org/10.3847/1538-4357/ab480d)
- Lichtenberg, T., Golabek, G. J., Burn, R., et al. 2019a, *Nat. Astron.*, 3, 307, doi: [10.1038/s41550-018-0688-5](https://doi.org/10.1038/s41550-018-0688-5)
- Lichtenberg, T., Golabek, G. J., Dullemond, C. P., et al. 2018, *Icarus*, 302, 27, doi: [10.1016/j.icarus.2017.11.004](https://doi.org/10.1016/j.icarus.2017.11.004)
- Lichtenberg, T., Golabek, G. J., Gerya, T. V., & Meyer, M. R. 2016, *Icarus*, 274, 350, doi: [10.1016/j.icarus.2016.03.004](https://doi.org/10.1016/j.icarus.2016.03.004)
- Lichtenberg, T., Keller, T., Katz, R. F., Golabek, G. J., & Gerya, T. V. 2019b, *Earth Planet. Sci. Lett.*, 507, 154, doi: [10.1016/j.epsl.2018.11.034](https://doi.org/10.1016/j.epsl.2018.11.034)
- Liu, B., & Ormel, C. W. 2018, *A&A*, 615, A138, doi: [10.1051/0004-6361/201732307](https://doi.org/10.1051/0004-6361/201732307)
- Liu, B., Ormel, C. W., & Johansen, A. 2019, *A&A*, 624, A114, doi: [10.1051/0004-6361/201834174](https://doi.org/10.1051/0004-6361/201834174)
- Lodders, K. 2003, *ApJ*, 591, 1220, doi: [10.1086/375492](https://doi.org/10.1086/375492)
- Lugaro, M., Ott, U., & Kereszturi, Á. 2018, *Prog. Part. Nucl. Phys.*, 102, 1, doi: [10.1016/j.pnpnp.2018.05.002](https://doi.org/10.1016/j.pnpnp.2018.05.002)
- Manara, C. F., Morbidelli, A., & Guillot, T. 2018, *A&A*, 618, L3, doi: [10.1051/0004-6361/201834076](https://doi.org/10.1051/0004-6361/201834076)
- Marchi, S., Walker, R. J., & Canup, R. M. 2020, *Sci. Adv.*, 6, eaay2338, doi: [10.1126/sciadv.aay2338](https://doi.org/10.1126/sciadv.aay2338)
- Marrocchi, Y., Bekaert, D. V., & Piani, L. 2018, *Earth Planet. Sci. Lett.*, 482, 23, doi: [10.1016/j.epsl.2017.10.060](https://doi.org/10.1016/j.epsl.2017.10.060)
- Marty, B. 2012, *Earth Planet. Sci. Lett.*, 313, 56, doi: [10.1016/j.epsl.2011.10.040](https://doi.org/10.1016/j.epsl.2011.10.040)
- Maurel, C., Bryson, J. F. J., Lyons, R. J., et al. 2020, *Sci. Adv.*, 6, eaba1303, doi: [10.1126/sciadv.aba1303](https://doi.org/10.1126/sciadv.aba1303)

- McCubbin, F. M., & Barnes, J. J. 2019, *Earth Planet. Sci. Lett.*, 526, 115771, doi: [10.1016/j.epsl.2019.115771](https://doi.org/10.1016/j.epsl.2019.115771)
- McKinney, W. 2010, in *Proceedings of the 9th Python in Science Conference*, ed. S. van der Walt & J. Millman, 51–56
- Mezger, K., Debaille, V., & Kleine, T. 2013, *SSRv*, 174, 27, doi: [10.1007/s11214-012-9935-8](https://doi.org/10.1007/s11214-012-9935-8)
- Mezger, K., Schönbachler, M., & Bouvier, A. 2020, *Space Sci. Rev.*, 216, 1
- Monteux, J., Golabek, G. J., Rubie, D. C., Tobie, G., & Young, E. D. 2018, *Space Sci. Rev.*, 214, 39, doi: [10.1007/s11214-018-0473-x](https://doi.org/10.1007/s11214-018-0473-x)
- Morbidelli, A., Bottke, W. F., Nesvorný, D., & Levison, H. F. 2009, *Icarus*, 204, 558, doi: [10.1016/j.icarus.2009.07.011](https://doi.org/10.1016/j.icarus.2009.07.011)
- Morbidelli, A., Lambrechts, M., Jacobson, S., & Bitsch, B. 2015, *Icarus*, 258, 418, doi: [10.1016/j.icarus.2015.06.003](https://doi.org/10.1016/j.icarus.2015.06.003)
- Morbidelli, A., Lunine, J. I., O'Brien, D. P., Raymond, S. N., & Walsh, K. J. 2012, *Annu. Rev. Earth Planet. Sci.*, 40, 251, doi: [10.1146/annurev-earth-042711-105319](https://doi.org/10.1146/annurev-earth-042711-105319)
- Morbidelli, A., Bitsch, B., Crida, A., et al. 2016, *Icarus*, 267, 368, doi: [10.1016/j.icarus.2015.11.027](https://doi.org/10.1016/j.icarus.2015.11.027)
- Najita, J. R., & Kenyon, S. J. 2014, *MNRAS*, 445, 3315, doi: [10.1093/mnras/stu1994](https://doi.org/10.1093/mnras/stu1994)
- Nakamura, T. 2006, *Earth Planet. Sci. Lett.*, 242, 26, doi: [10.1016/j.epsl.2005.11.040](https://doi.org/10.1016/j.epsl.2005.11.040)
- Nakato, A., Nakamura, T., Kitajima, F., & Noguchi, T. 2008, *Earth Planets Space*, 60, 855
- Nanne, J. A. M., Nimmo, F., Cuzzi, J. N., & Kleine, T. 2019, *Earth Planet. Sci. Lett.*, 511, 44, doi: [10.1016/j.epsl.2019.01.027](https://doi.org/10.1016/j.epsl.2019.01.027)
- Nesvorný, D., Li, R., Youdin, A. N., Simon, J. B., & Grundy, W. M. 2019, *Nat. Astron.*, 3, 808, doi: [10.1038/s41550-019-0806-z](https://doi.org/10.1038/s41550-019-0806-z)
- Nimmo, F., & Kleine, T. 2007, *Icarus*, 191, 497, doi: [10.1016/j.icarus.2007.05.002](https://doi.org/10.1016/j.icarus.2007.05.002)
- Nimmo, F., Kretke, K., Ida, S., Matsumura, S., & Kleine, T. 2018, *SSRv*, 214, 101, doi: [10.1007/s11214-018-0533-2](https://doi.org/10.1007/s11214-018-0533-2)
- Norris, C. A., & Wood, B. J. 2017, *Nature*, 549, 507, doi: [10.1038/nature23645](https://doi.org/10.1038/nature23645)
- Öberg, K. I., & Wordsworth, R. 2019, *AJ*, 158, 194, doi: [10.3847/1538-3881/ab46a8](https://doi.org/10.3847/1538-3881/ab46a8)
- Ormel, C. W., & Klahr, H. H. 2010, *A&A*, 520, A43, doi: [10.1051/0004-6361/201014903](https://doi.org/10.1051/0004-6361/201014903)
- Ormel, C. W., & Liu, B. 2018, *A&A*, 615, A178, doi: [10.1051/0004-6361/201732562](https://doi.org/10.1051/0004-6361/201732562)
- Paardekooper, S. J., Baruteau, C., Crida, A., & Kley, W. 2010, *MNRAS*, 401, 1950, doi: [10.1111/j.1365-2966.2009.15782.x](https://doi.org/10.1111/j.1365-2966.2009.15782.x)
- Paardekooper, S. J., Baruteau, C., & Kley, W. 2011, *MNRAS*, 410, 293, doi: [10.1111/j.1365-2966.2010.17442.x](https://doi.org/10.1111/j.1365-2966.2010.17442.x)
- Pape, J., Mezger, K., Bouvier, A. S., & Baumgartner, L. P. 2019, *GeoCoA*, 244, 416, doi: [10.1016/j.gca.2018.10.017](https://doi.org/10.1016/j.gca.2018.10.017)
- Pascucci, I., & Tachibana, S. 2010, in *Protoplanetary Dust: Astrophysical and Cosmochemical Perspectives*, ed. D. A. Apai & D. S. Lauretta, 263–298
- Pascucci, I., Testi, L., Herczeg, G. J., et al. 2016, *ApJ*, 831, 125, doi: [10.3847/0004-637X/831/2/125](https://doi.org/10.3847/0004-637X/831/2/125)
- Patočka, V., Calzavarini, E., & Tosi, N. 2020, *Phys. Rev. Fluids*, 5, 114304, doi: [10.1103/PhysRevFluids.5.114304](https://doi.org/10.1103/PhysRevFluids.5.114304)
- Peslier, A., Schönbachler, M., Busemann, H., & Karato, S.-I. 2018, *Space Sci. Rev.*, 212, 743
- Piani, L., Marrocchi, Y., Rigaudier, T., et al. 2020, *Science*, 369, 1110, doi: [10.1126/science.aba1948](https://doi.org/10.1126/science.aba1948)
- Piani, L., Yurimoto, H., & Remusat, L. 2018, *Nat. Astron.*, 2, 317, doi: [10.1038/s41550-018-0413-4](https://doi.org/10.1038/s41550-018-0413-4)
- Pignatale, F. C., Charnoz, S., Chaussidon, M., & Jacquet, E. 2018, *ApJL*, 867, L23, doi: [10.3847/2041-8213/aab22](https://doi.org/10.3847/2041-8213/aab22)
- Pirani, S., Johansen, A., Bitsch, B., Mustill, A. J., & Turrini, D. 2019, *A&A*, 623, A169, doi: [10.1051/0004-6361/201833713](https://doi.org/10.1051/0004-6361/201833713)
- Poole, G. M., Rehkämper, M., Coles, B. J., Goldberg, T., & Smith, C. L. 2017, *Earth Planet. Sci. Lett.*, 473, 215, doi: [10.1016/j.epsl.2017.05.001](https://doi.org/10.1016/j.epsl.2017.05.001)
- Raymond, S. N., Izidoro, A., & Morbidelli, A. 2020, in *Planetary Astrobiology*, ed. V. S. Meadows, G. N. Arney, B. E. Schmidt, & D. J. Des Marais (University of Arizona Press), 287
- Render, J., Brennecka, G. A., Wang, S.-J., Wasylenko, L. E., & Kleine, T. 2018, *ApJ*, 862, 26, doi: [10.3847/1538-4357/aacb7e](https://doi.org/10.3847/1538-4357/aacb7e)
- Rucska, J. J., & Wadsley, J. W. 2021, *MNRAS*, 500, 520, doi: [10.1093/mnras/staa3295](https://doi.org/10.1093/mnras/staa3295)
- Rudge, J. F., Kleine, T., & Bourdon, B. 2010, *Nat. Geosci.*, 3, 439, doi: [10.1038/ngeo872](https://doi.org/10.1038/ngeo872)
- Safronov, V. S. 1972, *Evolution of the protoplanetary cloud and formation of the earth and planets*.
- Sanborn, M. E., Wimpenny, J., Williams, C. D., et al. 2019, *GeoCoA*, 245, 577, doi: [10.1016/j.gca.2018.10.004](https://doi.org/10.1016/j.gca.2018.10.004)
- Sarafian, A. R., Nielsen, S. G., Marschall, H. R., McCubbin, F. M., & Monteleone, B. D. 2014, *Science*, 346, 623, doi: [10.1126/science.1256717](https://doi.org/10.1126/science.1256717)
- Sarafian, A. R., Hauri, E. H., McCubbin, F. M., et al. 2017, *Philos. Trans. R. Soc. A*, 375, 20160209, doi: [10.1098/rsta.2016.0209](https://doi.org/10.1098/rsta.2016.0209)
- Sato, T., Okuzumi, S., & Ida, S. 2016, *A&A*, 589, A15, doi: [10.1051/0004-6361/201527069](https://doi.org/10.1051/0004-6361/201527069)
- Schiller, M., Bizzarro, M., & Fernandes, V. A. 2018, *Nature*, 555, 507, doi: [10.1038/nature25990](https://doi.org/10.1038/nature25990)
- Schobert, B. N., Peeters, A. G., & Rath, F. 2019, *ApJ*, 881, 56, doi: [10.3847/1538-4357/ab2df6](https://doi.org/10.3847/1538-4357/ab2df6)
- Schönbachler, M., Carlson, R. W., Horan, M. F., Mock, T. D., & Hauri, E. H. 2010, *Science*, 328, 884, doi: [10.1126/science.1186239](https://doi.org/10.1126/science.1186239)

- Schoonenberg, D., & Ormel, C. W. 2017, *A&A*, 602, A21, doi: [10.1051/0004-6361/201630013](https://doi.org/10.1051/0004-6361/201630013)
- Scott, E. R. D., Krot, A. N., & Sanders, I. S. 2018, *ApJ*, 854, 164, doi: [10.3847/1538-4357/aaa5a5](https://doi.org/10.3847/1538-4357/aaa5a5)
- Segura-Cox, D. M., Schmiedeke, A., Pineda, J. E., et al. 2020, *Nature*, 586, 228, doi: [10.1038/s41586-020-2779-6](https://doi.org/10.1038/s41586-020-2779-6)
- Shakura, N. I., & Sunyaev, R. A. 1973, *A&A*, 24, 337
- Simon, J. B., Armitage, P. J., Li, R., & Youdin, A. N. 2016, *ApJ*, 822, 55, doi: [10.3847/0004-637X/822/1/55](https://doi.org/10.3847/0004-637X/822/1/55)
- Simon, J. B., Armitage, P. J., Youdin, A. N., & Li, R. 2017, *ApJL*, 847, L12, doi: [10.3847/2041-8213/aa8c79](https://doi.org/10.3847/2041-8213/aa8c79)
- Singer, K. N., McKinnon, W. B., Gladman, B., et al. 2019, *Science*, 363, 955, doi: [10.1126/science.aap8628](https://doi.org/10.1126/science.aap8628)
- Sossi, P. A., Klemme, S., O'Neill, H. S. C., Berndt, J., & Moynier, F. 2019, *GeoCoA*, 260, 204, doi: [10.1016/j.gca.2019.06.021](https://doi.org/10.1016/j.gca.2019.06.021)
- Stevenson, D. J., & Lunine, J. I. 1988, *Icarus*, 75, 146, doi: [10.1016/0019-1035\(88\)90133-9](https://doi.org/10.1016/0019-1035(88)90133-9)
- Sutton, S., Alexander, C. M. O., Bryant, A., et al. 2017, *GeoCoA*, 211, 115, doi: [10.1016/j.gca.2017.05.021](https://doi.org/10.1016/j.gca.2017.05.021)
- Teague, R., Bae, J., & Bergin, E. A. 2019, *Nature*, 574, 378, doi: [10.1038/s41586-019-1642-0](https://doi.org/10.1038/s41586-019-1642-0)
- Teague, R., Guilloteau, S., Semenov, D., et al. 2016, *A&A*, 592, A49, doi: [10.1051/0004-6361/201628550](https://doi.org/10.1051/0004-6361/201628550)
- Toth, E. R., Fehr, M. A., Friebe, M., & Schönbächler, M. 2020, *GeoCoA*, 274, 286, doi: [10.1016/j.gca.2020.01.059](https://doi.org/10.1016/j.gca.2020.01.059)
- Trinquier, A., Birck, J.-L., & Allègre, C. J. 2007, *ApJ*, 655, 1179, doi: [10.1086/510360](https://doi.org/10.1086/510360)
- Trinquier, A., Elliott, T., Ulfbeck, D., et al. 2009, *Science*, 324, 374, doi: [10.1126/science.1168221](https://doi.org/10.1126/science.1168221)
- Tsirvoulis, G., Morbidelli, A., Delbo, M., & Tsiganis, K. 2018, *Icarus*, 304, 14, doi: [10.1016/j.icarus.2017.05.026](https://doi.org/10.1016/j.icarus.2017.05.026)
- Turner, N. J., Fromang, S., Gammie, C., et al. 2014, in *Protostars and Planets VI*, ed. H. Beuther, R. S. Klessen, C. P. Dullemond, & T. Henning, 411, doi: [10.2458/azu_uapress_9780816531240-ch018](https://doi.org/10.2458/azu_uapress_9780816531240-ch018)
- Tychoniec, Ł., Manara, C. F., Rosotti, G. P., et al. 2020, *A&A*, 640, A19, doi: [10.1051/0004-6361/202037851](https://doi.org/10.1051/0004-6361/202037851)
- van Dishoeck, E. F., Bergin, E. A., Lis, D. C., & Lunine, J. I. 2014, in *Protostars and Planets VI*, ed. H. Beuther, R. S. Klessen, C. P. Dullemond, & T. Henning, 835, doi: [10.2458/azu_uapress_9780816531240-ch036](https://doi.org/10.2458/azu_uapress_9780816531240-ch036)
- Van Kooten, E. M. M. E., Wielandt, D., Schiller, M., et al. 2016, *Proc. Natl. Acad. Sci. U.S.A.*, 113, 2011, doi: [10.1073/pnas.1518183113](https://doi.org/10.1073/pnas.1518183113)
- Virtanen, P., Gommers, R., Oliphant, T. E., et al. 2020, *Nat. Methods*, 17, 261, doi: [10.1038/s41592-019-0686-2](https://doi.org/10.1038/s41592-019-0686-2)
- Visser, R. G., & Ormel, C. W. 2016, *A&A*, 586, A66, doi: [10.1051/0004-6361/201527361](https://doi.org/10.1051/0004-6361/201527361)
- Wada, K., Tanaka, H., Suyama, T., Kimura, H., & Yamamoto, T. 2009, *ApJ*, 702, 1490, doi: [10.1088/0004-637X/702/2/1490](https://doi.org/10.1088/0004-637X/702/2/1490)
- . 2011, *ApJ*, 737, 36, doi: [10.1088/0004-637X/737/1/36](https://doi.org/10.1088/0004-637X/737/1/36)
- Wang, H., Weiss, B. P., Bai, X.-N., et al. 2017, *Science*, 355, 623, doi: [10.1126/science.aaf5043](https://doi.org/10.1126/science.aaf5043)
- Warren, P. H. 2011, *Earth Planet. Sci. Lett.*, 311, 93, doi: [10.1016/j.epsl.2011.08.047](https://doi.org/10.1016/j.epsl.2011.08.047)
- Waskom, M., & the seaborn development team. 2020, *mwaskom/seaborn*, latest, Zenodo, doi: [10.5281/zenodo.592845](https://doi.org/10.5281/zenodo.592845)
- Williams, C. D., & Mukhopadhyay, S. 2019, *Nature*, 565, 78, doi: [10.1038/s41586-018-0771-1](https://doi.org/10.1038/s41586-018-0771-1)
- Wu, J., Desch, S. J., Schaefer, L., et al. 2018, *J. Geophys. Res. Planet.*, 123, 2691, doi: [10.1029/2018JE005698](https://doi.org/10.1029/2018JE005698)
- Yang, L., & Ciesla, F. J. 2012, *Meteorit. Planet. Sci.*, 47, 99, doi: [10.1111/j.1945-5100.2011.01315.x](https://doi.org/10.1111/j.1945-5100.2011.01315.x)
- Youdin, A. N., & Goodman, J. 2005, *ApJ*, 620, 459, doi: [10.1086/426895](https://doi.org/10.1086/426895)
- Young, E. D., Ash, R. D., England, P., & Rumble, D., I. 1999, *Science*, 286, 1331, doi: [10.1126/science.286.5443.1331](https://doi.org/10.1126/science.286.5443.1331)